Nano Research

ISSN 1998-0124 CN 11-5974/O4
https://doi.org/10.26599/NR.2026.94908543

Research Article

Wafer-scale interface-clean few-layer graphene stacks enabled by active oxygen treatment

Siyi Ji[1,2,§], Xin Gao[3,§], Zhilong Shang[4,5,§], Weiyu Sun[3,6], Xiaoyin Gao[3], Kaicheng Jia[2], Mengwei Li[1], Junqiang Wang[1], Hongtao Liu[3](✉), Fang Luo[4,5](✉), Hailin Peng[2,3](✉)

[1] Academy for Advanced Interdisciplinary Research, North University of China, Taiyuan 030051, China

[2] Beijing Graphene Institute, Beijing 100095, China

[3] Center for Nano chemistry, Beijing Science and Engineering Center for Nanocarbons, Beijing National Laboratory for Molecular Sciences, College of Chemistry and Molecular Engineering, Peking University, Beijing 100871, China

[4] College of Advanced Interdisciplinary Studies& Hunan Provincial Key Laboratory of Novel Nano-optoelectronic Information Materials and Devices, National University of Defense Technology, Changsha 410073, China

[5] Nanhu Laser Laboratory, National University of Defense Technology, Changsha 410073, China

[6] Academy for Advanced Interdisciplinary Studies, Peking University, Beijing 100871, China

[§] Siyi Ji, Xin Gao, and Zhilong Shang contributed equally to this work.

Nano Res., **Just Accepted Manuscript** • https://doi.org/10.26599/NR.2026.94908543

https://www.sciopen.com/journal/1998-0124 on Feb. 6, 2026

TABLE OF CONTENTS (TOC)

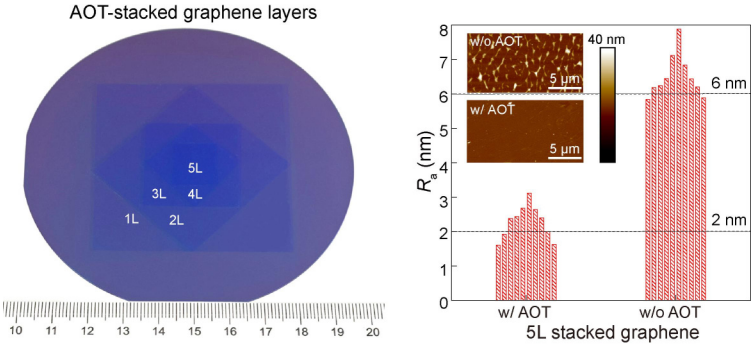

An active oxygen treatment (AOT) strategy was developed to effectively remove surface impurities and amorphous carbon on graphene before stacking, yielding wafer-scale few-layer graphene with clean interface and controlled layer numbers.

Nano Research

Open Access

Research Article

Wafer-scale interface-clean few-layer graphene stacks enabled by active oxygen treatment

Siyi Ji[1,2,§], Xin Gao[3,§], Zhilong Shang[4,5,§], Weiyu Sun[3,6], Xiaoyin Gao[3], Kaicheng Jia[2], Mengwei Li[1], Junqiang Wang[1], Hongtao Liu[3*], Fang Luo[4,5*], and Hailin Peng[2,3*]

[1] *Academy for Advanced Interdisciplinary Research, North University of China, Taiyuan 030051, China*
[2] *Beijing Graphene Institute, Beijing 100095, China*
[3] *Center for Nano chemistry, Beijing Science and Engineering Center for Nanocarbons, Beijing National Laboratory for Molecular Sciences, College of Chemistry and Molecular Engineering, Peking University, Beijing 100871, China*
[4] *College of Advanced Interdisciplinary Studies& Hunan Provincial Key Laboratory of Novel Nano-optoelectronic Information Materials and Devices, National University of Defense Technology, Changsha 410073, China*
[5] *Nanhu Laser Laboratory, National University of Defense Technology, Changsha 410073, China*
[6] *Academy for Advanced Interdisciplinary Studies, Peking University, Beijing 100871, China*
[§] *Siyi Ji, Xin Gao, and Zhilong Shang contributed equally to this work.*

Received: 17 October 2025; **Revised:** 14 January 2026; **Accepted:** 6 February 2026

Address correspondence to Hongtao Liu, htliu-cnc@pku.edu.cn; Fang Luo, luofang@nudt.edu.cn; Hailin Peng, hlpeng@pku.edu.cn

Cite this article: *Nano Research*, **2026**, *19*, 94908543. https://doi.org/10.26599/NR.2026.94908543

ABSTRACT: Interface quality, one of critical factors, governs the properties of few-layer graphene, which exhibit exclusive electrical and mechanical properties owing to the strong interlayer coupling. However, fabrication of interface-clean few-layer graphene still remains challenging. Conventional stacking techniques often introduce interfacial contamination, such as amorphous carbon and residual impurities, which critically deteriorate the interlayer coupling and compromise the uniformity and reliability of graphene-based devices. Here, we present an active oxygen treatment (AOT) strategy to effectively remove surface impurities and amorphous carbon on graphene before stacking, yielding wafer-scale few-layer graphene with clean interface and controlled layer numbers. As-fabricated few-layer graphene exhibits excellent structural integrity (>95%), flatness (R_a ~ 2.3 nm) and uniformity. The suspended few-layer graphene shows superior mechanical stability due to the clean interface, which remains stable under repeated thermal shocks up to 1200 K, significantly outperforming counterparts assembled via conventional methods. Thermal light emitters based on the suspended few-layer graphene demonstrates strong visible-to-near-infrared emission, with lattice temperature reaches ~900 K and a working lifetime of ~70 min. This work highlights the potential of AOT in advancing the optoelectronic applications of graphene through precise interface engineering.

KEYWORDS: few-layer graphene, active oxygen treatment, interface modulation, suspended graphene, thermal emitters

1 Introduction

Few-layer graphene (FLG) exhibits unique properties that differ significantly from both monolayer graphene and bulk graphite, depending strongly on the number of layers and stacking order. Monolayer graphene is a gapless semimetal with ultrahigh carrier mobility arising from its Dirac cone band structure[1]. In contrast, bilayer and few-layer graphene possess twist angle-tunable band structures and exhibit emergent properties[2–5]. FLG also demonstrates outstanding mechanical strength, high electrical mobility, broadband optical absorption, and ultrahigh thermal conductivity[6–10], making it attractive for high-performance electronic and optoelectronic devices[11,12]. Moreover, FLG hosts a range of emergent quantum phenomena, including correlated insulating states, superconductivity, and ferromagnetism, enabled by flat bands and enhanced electron interactions, positioning it as a versatile platform for exploring strongly correlated physics[13–16].

To realize these exceptional properties, high-quality FLG with atomically clean interfaces and well-controlled layer number are highly required. However, existing fabrication methods still suffer significant limitations. Mechanical exfoliation yields high-quality flakes but with random layer numbers and limited lateral size[17,18]. Chemical vapor deposition (CVD) enables large-area synthesis but struggles to precisely control layer number and stacking order[19,20]. Epitaxial growth of graphene on SiC offers layer number uniformity but requires high temperatures and has limited substrate compatibility[21,22]. Layer-by-layer (LBL) stacking offers precise control over layer number, large area and stacking order, yet suffers from interfacial contamination, such as amorphous carbon, polymer residues, and adsorbates[23]. Interfacial contamination induces interfacial bubbles that obscure intrinsic properties and degrade interlayer coupling[24–26]. To remove the interfacial contamination trapped between stacked graphene layers, previous works have shown that mechanical quizzing and post-annealing are effective and can be used to reduce bubbles[27–31], but these methods are either complex or time-consuming. Backside lamination strategy

enables bubble-free bilayer graphene but are difficult to scale to fabricate multilayers[32]. Thus, a reliable, wafer-scale, and interface-clean method for assembling high-quality FLG remains a key challenge for both fundamental studies and practical device applications.

Here, a simple but effective stacking method based on active oxygen treatment (AOT) has been developed to fabricate wafer-scale interface-clean few-layer graphene. The active oxygen treatment is introduced before stacking to remove the amorphous carbon and adsorbed impurities on the graphene surface, resulting in clean and uniform interfaces. Based on the AOT transfer method, a uniform large-area five-layer graphene with high structural integrity has been successfully fabricated, exhibiting a flatter surface and cleaner interfaces compared to that fabricated by conventional LBL stacking. Moreover, due to the clean interface, the few-layer graphene stacks on holey substrate shows excellent mechanical stability, withstanding repeated thermal shocks up to 1200 K without degradation. Finally, light-emitting devices based on the AOT-stacked graphene demonstrate strong visible-to-near-infrared emission (lattice temperature~900 K) and a long working lifetime of approximately 70 min. This work shows the potential of active oxygen treatment as a powerful interface engineering technique to facilitate the integration of graphene into next-generation optoelectronic applications.

2 Results and discussion

Single-crystal graphene films grown on Cu (111)/sapphire substrates were employed in this study to fabricate few-layer graphene, owing to their atomically flat surfaces[33–35]. To enable high-quality layer-by-layer stacking, a multilayer transfer medium was designed, allowing individual monolayer graphene to be delaminated and assembled sequentially (Fig. 1a and Fig. S1). A critical prerequisite for achieving clean interfaces in stacked graphene is the effective removal of surface contaminants prior to lamination. Consequently, active oxygen generated via O_2 plasma was applied to the graphene surfaces before lamination, producing clean surfaces suitable for high-quality stacking. In details, the transfer medium consists of polydimethylsiloxane (PDMS), poly (methyl methacrylate) (PMMA), poly (propylene carbonate) (PPC), and borneol, collectively enabling the intact and contamination-free transfer of wafer-scale graphene. Specifically, PDMS serves as a self-supporting layer to handle and dry-stack graphene layers. PMMA offers mechanical support to maintain the structural integrity of graphene during transfer process. PPC acts as a flexible layer to ensure conformal contact of graphene onto target substrate[36]. Borneol, a small-molecule interlayer, prevents polymer contamination, thereby preserving clean graphene surface[33]. Importantly, AOT effectively removes amorphous carbon and adsorbed hydrocarbons from graphene surfaces, ensuring the conformal contact of graphene layers and yielding an ultra-flat, bubble-free interface. The detailed AOT treatment parameters can be found in Method and Fig. S2 to S4. Note that, the graphene would be slightly functionalized after controlled AOT (Fig. S5), showing an $I_D/I_G \sim 0.13$.

Based on the designed AOT method, large-area interface-clean few-layer graphene have been successfully stacked and transferred on SiO_2/Si (Fig. 1b). Optical image of the AOT-stacked graphene with different layers exhibits distinct contrast, which enhances with increased layer numbers and remains uniform within the same layer number regions, indicating

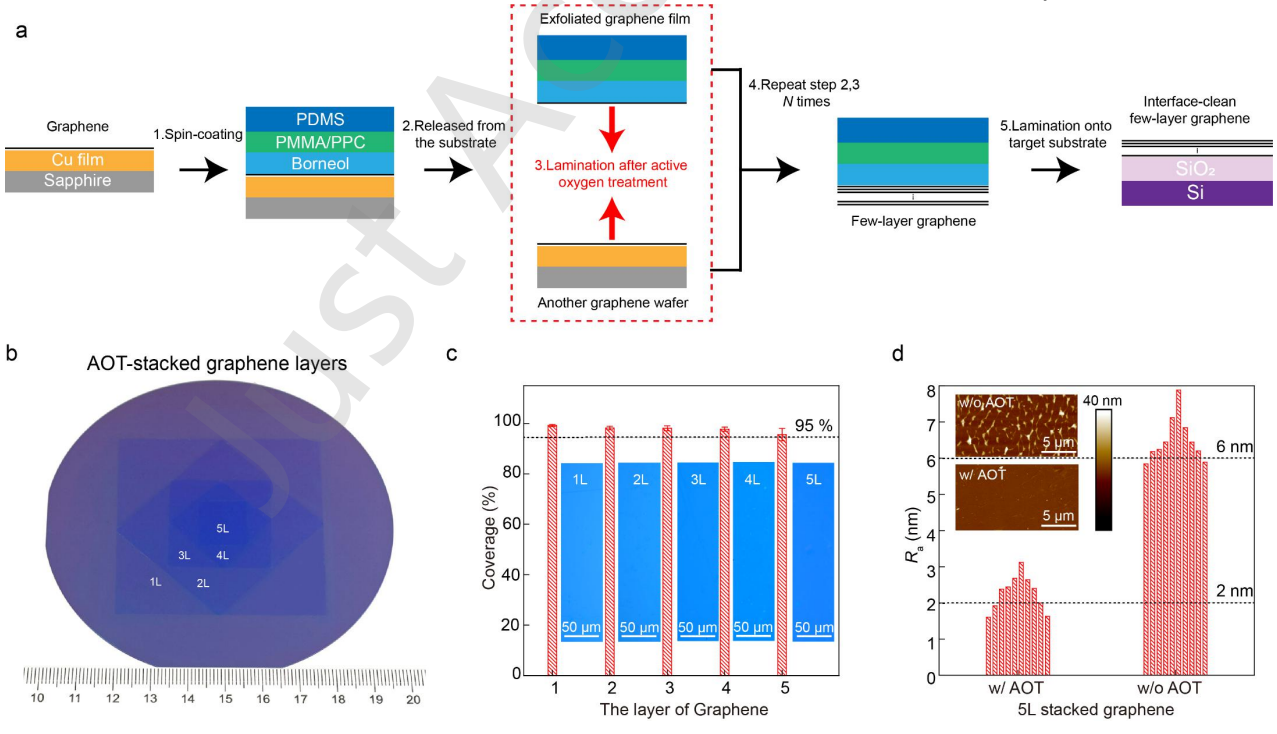

Fig. 1 | Fabrication of stacked large-area few-layer graphene via active oxygen treatment. (**a**) Schematic illustration of active oxygen assisted fabrication of few-layer graphene. The key step is active oxygen treatment (AOT), after which fresh and clean graphene surfaces are formed and immediately dry-laminated. (**b**) Photograph of AOT-stacked large-area few-layer graphene on a SiO_2/Si substrate. (**c**) Histograms of coverage of AOT-stacked monolayer to five-layer graphene. Inset: Optical microscopy images of different layer graphene. (**d**) Histograms of roughness of five-layer graphene stacked with and without AOT collected from 10 × 10 μm^2 AFM images. Inset: AFM images of five-layer graphene stacked with and without AOT.

consistent layer thickness and clean interfaces throughout the few-layer graphene stacks. The microscopy optical images (inset of Fig. 1c and Fig. S6) indicate that there are no optically visible interface-bubbles in AOT-stacked graphene, while the conventional LBL-stacked graphene shows dense interface-bubbles (Fig. S7 and Fig. S8). Optical characterization confirms that the coverage of the transferred different-layer graphene all exceeds 95%. From monolayer to five-layer, the coverage values are 99.1%, 98.2%, 98%, 97.7%, and 95.6%, respectively, demonstrating high stacking uniformity and integrity. Benefiting from the clean interface, the stacked five-layer graphene exhibits a bubble-free and flat surface with a surface roughness (R_a) of ~ 2.3 nm (Fig. 1d). On the contrary, the LBL-transferred five-layer graphene exhibits large surface roughness (R_a ~ 6.5 nm) with dense bubbles and wrinkles. The low roughness and absence of interfacial bubbles of AOT-stacked few-layer films would ensure the superior electrical and mechanical properties of graphene.

The uniformity is important for the devices based on few-layer graphene stacks. To assess the macroscopic uniformity of the AOT-stacked few-layer graphene, the sheet resistance of the large-area stacked film shown in Fig. 1b was measured. As presented in Fig. 2a, the sheet resistance decreases with increasing layer number and exhibits a uniform distribution across the sample with the same layer numbers. Notably, the five-layer graphene in the central region shows the lowest sheet resistance, with R_s ~ 220 Ω/sq. The sheet resistance decreased due to the increased conductive paths and interlayer coupling in few-layer graphene, which has high carrier density, enhanced charge screening and suppressed carrier scattering[37,38]. By comparison, the sheet resistance map of LBL-stacked few-layer graphene exhibits a poor uniformity and a relatively large resistance in the central 5-layer region (~260 Ω/sq), which is presumably caused by the poor structural integrity and inferior interlayer quality (Fig. S9). Raman spectroscopy was also collected to analyze the microscopic uniformity, including the layer variations and interlayer coupling in few-layer graphene[39–43]. The Raman spectra of AOT-stacked graphene exhibit typical layer-dependent evolution of I_G/I_{2D} ratio, confirming the consistent layer number of few-layer graphene stacks (Fig. S10). Raman mapping images collected from 9 positions of the AOT-stacked five-layer graphene are uniform, indicating the few-layer graphene stacks has a uniform layer number and interlayer coupling. (Fig. 2b). Note that, the uniform and flat morphology of AOT-stacked graphene show a higher carrier mobility than LBL-stacked graphene with dense interfacial bubbles due to the reduced carrier scattering (Fig. S11).

Furthermore, scanning electron microscopy (SEM) and transmission electron microscopy (TEM) were employed to evaluate the interfacial cleanness of the few-layer graphene stacks. As shown in SEM images (Fig. S12), the density of interfacial bubbles in AOT-stacked graphene is significantly lower than that in LBL-stacked graphene, indicating a much cleaner interface achieved through the AOT process. TEM images further confirm the bubble-free interface with minimal residue of AOT-stacked graphene, whereas LBL-stacked graphene exhibits substantial contaminant aggregate within the interfacial bubbles (Fig. 2c and Fig. S13). Additionally, selected-area electron diffraction (SAED) patterns of the AOT-stacked five-layer graphene display five distinct sets of

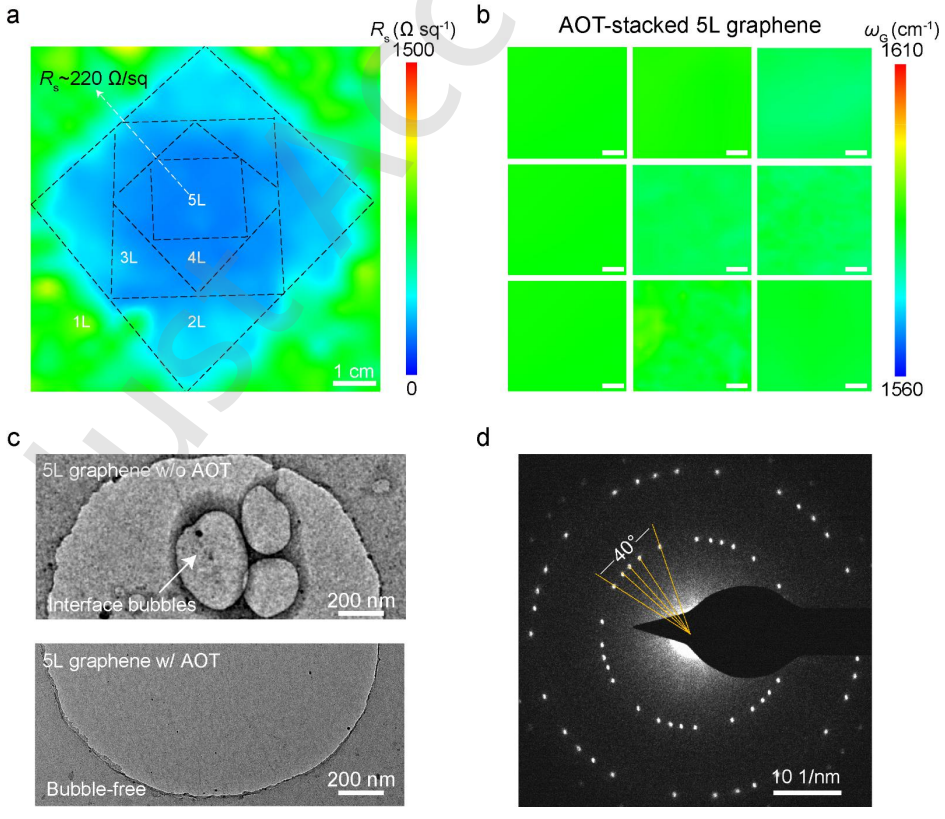

Fig. 2 | Uniformity and cleanliness of AOT-stacked few-layer graphene. (**a**) Sheet resistance mapping of AOT-stacked few-layer graphene. The average sheet resistance of the five-layer region is 220 Ω sq^{-1}. (**b**) Raman mapping images of AOT-stacked five-layer graphene. Scale bars are 5 μm. (**c**) TEM images of five-layer graphene stacked with and without AOT. The areas indicated by the white arrow represent interfacial bubbles. (**d**) SAED of AOT-stacked five-layer graphene.

diffraction spots, confirming the successful stacking of five monolayers with preserved crystallinity and alignment (Fig. 2d). These results demonstrate the effectiveness of AOT in achieving atomically clean graphene interfaces, which are critical for high-performance electronic and optoelectronic applications.

The AOT-stacked few-layer graphene can also be transferred onto holey substrates, enabling the fabrication of wafer-scale, interface-clean suspended few-layer graphene (Fig. 3a) with no visible damage under both 20× and 100× optical microscope (Fig. 3b). Benefiting from the clean interface, the stacked few-layer suspended graphene preserves the structural integrity, indicating its exceptional mechanical property. Notably, the AOT-stacked few-layer graphene can be transferred onto a variety of holey substrates with diverse shapes and dimensions (Fig. 3c, 3d and Fig. S14). As shown in Fig. 3c, the structural integrity of the suspended few-layer graphene increases with the layer number. The five-layer graphene achieves a coverage of approximately 92.3% on 5 μm-diameter circular holes, indicating its excellent mechanical robustness. Even when the suspended area increases to 120 μm^2, the AOT-stacked five-layer graphene retains a high coverage of around 88.6%, while the integrity of monolayer is only ~5% on a 30 μm^2 suspended area. Note that, the PPC in our designed transfer medium is vital to ensure the conformal contact of few-layer graphene onto holey substrates (Fig. S14a).

Mechanical stability is a critical parameter for the reliable application of suspended graphene in high-temperature environments[44,45]. To evaluate the mechanical stability of few-layer graphene stacks under high temperature, thermal shock tests were conducted on suspended bilayer stacked graphene assembled via both AOT and conventional LBL methods. The tests were performed in vacuum, with the samples subjected to 100 rapid thermal cycles between 800 K and 1200 K. The heating rate, derived from the temperature-time slope shown in Fig. 3e, was approximately 4000 K/s. The results reveals that the AOT-stacked bilayer graphene retains ~86.4% of its structural integrity after test, while the LBL-stacked counterpart showed a significant decline, maintaining only ~62.7% integrity (Fig. 3f and Fig. S15). The inferior performance of the LBL-stacked sample is attributed to the poor interface coupling and presence of interfacial bubbles, which trapped impurities and induce localized stress during rapid heating, ultimately leading to the fracture. In contrast, AOT-stacked few-layer graphene exhibits superior mechanical stability mainly benefiting from the absence of interfacial bubbles and the enhanced interlayer coupling.

To further demonstrate the advantages of AOT-stacked few-layer graphene for device applications, high-performance suspended-graphene light-emitting devices were successfully fabricated (Fig. 4a). AOT-stacked five-layer graphene was used as the suspended emitter due to its high emissivity and superior mechanical robustness. In details, AOT-stacked five-layer graphene was transferred onto trench pattern substrates (Fig. 4b),

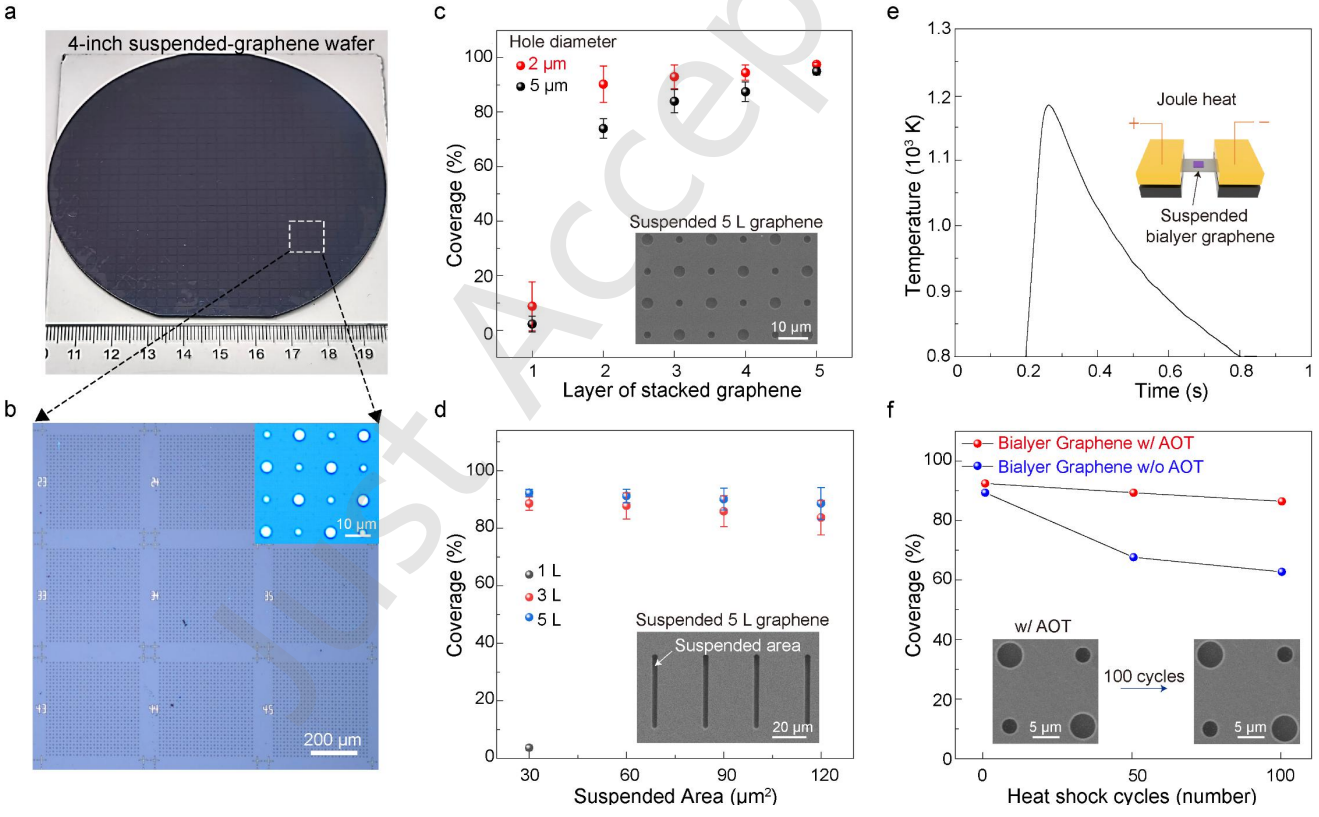

Fig. 3 | Wafer-scale suspended few-layer graphene and its thermal shock stability. (**a**) Photograph of bilayer graphene transferred on a 4-inch holey SiO_2/Si substrate by AOT-method. (**b**) Optical microscopy image of bilayer graphene on the holey SiO_2/Si substrate. Inset: Enlarged optical microscopy image of the suspended bilayer graphene. The white holes are covered by bilayer graphene. (**c**) Statistic coverage of monolayer to five layers graphene on 2 μm and 5 μm diameter circular holes. Inset: SEM image of five-layer graphene on SiO_2/Si substrate with circular holes. Dark regions are the holes. (**d**) Statistic coverage of monolayer, three-layer, five-layer graphene on SiO_2/Si substrate with round slot holes. Inset: SEM image of the five-layer graphene. (**e**) Temperature curve of a single thermal shock. Inset: The diagram of a thermal shock device. Heating is achieved via Joule heating, with a carbon felt placed between the electrodes to support the silicon wafer carrying the transferred suspended graphene. (**f**) Coverage of bilayer graphene stacked with and without AOT after 100 thermal shock cycles. Inset: SEM images of the bilayer graphene stacked by AOT-method before and after thermal shock.

followed by the fabrication of two-terminal devices[46,47]. Upon current injection through the suspended graphene channel, Joule heating induces thermal radiation, resulting in visible-to-near-infrared light emission. As shown in Fig. 4c, the graphene light emitter exhibits bright visible emission under optical microscope.

The radiation spectra reveal that the emission spans the visible to near-infrared range (Fig. 4d), with the intensity increasing significantly with applied bias, indicating efficient thermal radiation. The thermal radiation efficiency of the suspended five-layer graphene device was calculated to be 3.85×10^{-4} (Fig. S16). The lattice temperature of the AOT-stacked five-layer graphene, collected from the shift of the Raman G-band under electrical bias[48] (Fig. S17), reaches approximately 885 K at a power density of 7.04 kW cm^{-2} under vacuum (Fig. 4e). The input power density is considerably lower than the values reported in the literature[49,50] (Table S1), mainly benefited by the AOT-stacked interface-clean five-layer suspended graphene. Higher power densities are expected to further raise the lattice temperature, demonstrating the potential of this platform for developing high-brightness light-emitting devices integrated on silicon substrates. Furthermore. graphene emitters with different dimensions (length and width) were fabricated, which could also emit near-infrared and visible light once the applied voltage exceeds a certain threshold (Fig. S18). In addition, device reliability was evaluated under prolonged operation. The suspended five-layer graphene light emitter operated continuously for approximately 70 minutes at a power density of 7.29 kW cm^{-2} (corresponding to a temperature exceeding 900 K) before electrical breakdown. The radiation spectra remain relatively stable within at least 40 min due to the clean interface of AOT-stacked graphene. (Fig. S19). Notably, this stable operation was achieved without any encapsulation (Fig. 4f), highlighting the robustness of the AOT-stacked structure and its suitability for high-temperature, long-lifetime optoelectronic applications.

3 Conclusion

In summary, a simple but effective AOT method was developed to fabricate larger-area interface-clean few-layer graphene stacks. By introducing AOT prior to stacking, surface impurities and amorphous carbon are effectively removed, resulting in clean graphene interfaces. The stacked graphene films exhibit excellent flatness (R_a ~2.3 nm), high structural integrity (>95% coverage), and uniform electrical and Raman properties across large areas. Moreover, the stacked interface-clean few-layer graphene could also be transferred onto various holey substrates, yielding few-layer suspended graphene with minimal damage or wrinkling due to its exceptional mechanical robustness. Notably, AOT-stacked suspended graphene retains structural integrity under repeated thermal shock cycles up to 1200 K, significantly outperforming films assembled by conventional layer-by-layer methods. Additionally, we demonstrated light-emitting devices based on suspended five-layer graphene that exhibit strong visible-to-near-infrared emission and a prolonged operational lifetime (~70 min), highlighting the potential of this method for high-performance optoelectronic applications. The AOT

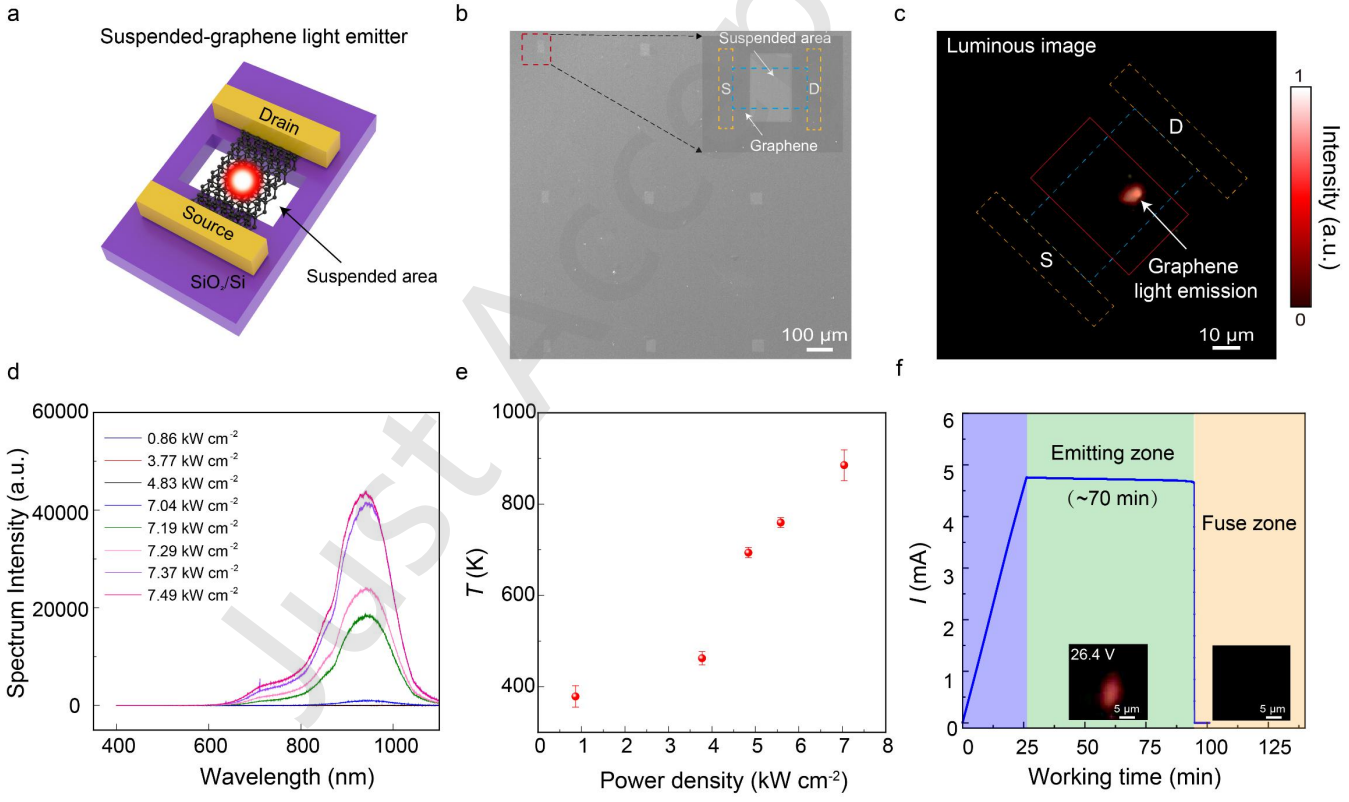

Fig. 4 | Light emission of suspended five-layer graphene. (**a**) Schematic diagram of the suspended-graphene light emitter. (**b**) SEM image of suspended five-layer graphene arrays fabricated by AOT-method. Inset image indicates the graphene channel, suspended area, source and drain electrodes. (**c**) Image of light emission at P = 7.49 kW cm^{-2} captured by a microscope camera. The blue dashed line and yellow dashed line indicate the graphene channel and metal electrodes, respectively. The red box represents suspended area. (**d**) Emission spectra collected from a graphene emitter at various input power. (**e**) Graphene lattice temperatures obtained by the shift in Raman G peak's position. (**f**) Long-term stability test of the device. The purple, green, and orange periods represent the voltage ramp-up, the light-emitting stage at 7.29 kW cm^{-2}, and the fusing stage, respectively. Inset images indicate the light emission during the emitting and fusing periods. the scale bar is 5 μm.

stacking method would be compatible for constructing bubble-free 2D van der Waals homo/hetero-structures, facilitating the application of 2D materials in electronic and photonic devices.

4 Method

Transfer of bubble-free few-layer graphene using the AOT method: Ultra-flat single-crystal graphene was by provided Beijing Graphene Research Institute[35]. A step-by-step transfer protocol is available in Supplementary Information. First, the graphene wafer was cut into two pieces and the cut lines were assigned as the positioning edge to control the twisted angle. Then, transfer mediums were deposited on the first pieces of graphene. A layer of Borneol (>97% purity, Alfa Aesar) was spin-coated at 2000 rpm for 1 min from an isopropyl alcohol solution (25 wt%) and baked at 80 ℃ for 3 min. Then PPC film (300 nm thick) was spin-coated on the borneol layer at 2000 rpm for 1 min from 0.1 g mL^{-1} anisole solution of PPC (Mw = 20w, Empower Materials), and baked at 80 ℃ for 3 min. PMMA (950K A4, Microchem Inc.) film was spin-coated on the PPC layer at 2000 rpm for 1 min, then baked at 170 ℃ for 5 min. Finally, PDMS (WF-40×40-0060-X4, Gel-Pak) was attached on the PMMA thin film to obtain the PDMS/PMMA/PPC/Borneol/graphene/Cu (111) /sapphire composite structure. Graphene was detached from the growth substrate by an electrochemical bubbling method in 1 mol L^{-1} NaOH (Rawhn, Shanghai Yien Chemical Technology Co., Ltd) aqueous solution[51]. Washing with deionized water removes residual solution. After rinsing and drying, the bottom surface of the delaminated graphene and the top surface of another graphene sheet were simultaneously treated in a plasma cleaner (Diener, pico) using active oxygen at 30 W for 42 s at an oxygen flow rate of 5 sccm under a pressure of 0.1 mbar. Then, the two treated graphene were laminated together with a commercial laminator (LM-330ID, Rayson Co., Ltd), followed by baking at 180 ℃ for 5 min to release upper PDMS layer and promote conformal contact of the graphene layers. For subsequent stacking, in order to fabricate a self-supporting composite film, another PDMS layer must be laminated onto the PMMA support to facilitate the following stacking process. After stacking, the PDMS was detached from the PMMA thin film to obtain the PMMA/PPC/Borneol/BLG/Cu (111)/sapphire composite structure. And a new PDMS layer was attached on the PMMA thin film to obtain the PDMS/PMMA/PPC/Borneol/BLG/Cu (111)/sapphire composite structure. The bilayer graphene was detached from the growth substrate by an electrochemical bubbling method. Repeating the previous AOT, stacking, delamination, rinsing and drying steps obtained a PDMS/PMMA/PPC/Borneol/few-layer graphene film, and then the film was transferred onto the target substrate, such as SiO_2/Si. The PDMS was peeled off from PMMA at 180 °C leaving the PMMA/PPC/Borneol/few-layer graphene on the substrate, which was then baked at 180 °C for 2 h. Finally, PMMA, PPC and borneol was removed with the vapor of hot acetone, obtaining the few-layer graphene on the target substrate.

Transfer and stack of few-layer graphene by conventional LBL method: The scheme of the conventional LBL transfer process is shown in Fig. S3. First, PMMA was spin-coated on one piece of graphene/Cu (111)/sapphire at 2000 rpm for 1 min, and baked at 170 °C for 5 min. PDMS was laminated on the PMMA/graphene/Cu (111)/sapphire sample. After that, PDMS/PMMA/graphene film was detached from the growth substrate by electrochemical bubbling delamination in 1 mol L^{-1} NaOH aqueous solution. After washing off the residual electrolyte with deionized water, the composite film was dried in air at room temperature, followed by laminating onto the second piece of graphene/Cu (111)/sapphire. Repeating the previous stacking, delamination, rinsing and drying steps obtained a PDMS/PMMA/few-layer graphene film, and then the film was transferred onto SiO_2/Si substrate. The PDMS was peeled off from PMMA at 180 °C, and the PMMA/few-layer graphene/SiO_2/Si was baked at 180 °C for 2 h. Finally, the PMMA was removed with the vapor of hot acetone, leaving the few-layer graphene on the target substrate.

Fabrication of suspended graphene light emitting devices: Various trench patterns were etched on a SiO_2/Si substrate with ultraviolet lithography (SUSS MicroTec, MA6/BA6) and ICP etching (Leuven instruments). Then the patterns were filled with a sacrificial material. For getting a flat surface, we polished the surface of the substrate used a mechanical polishing machine (FEMΛ GRINDING and POLISHING). After that, the AOT-stacked five-layer graphene was transferred onto the substrate. Then, electrodes were fabricated through ultraviolet lithography (SUSS MicroTec, MA6/BA6) and electron beam evaporation (TECHNOL, TEMD500). Immediately after that, we used ultraviolet lithography SUSS MicroTec, MA6/BA6) and oxygen plasma etching (Sanhoptt, PT-5ST) to define the graphene channels. Finally, the sacrificial material filled in the holes was removed and the suspended-graphene light emitting devices were completed.

Characterization: Optical microscopy images were collected on a Nikon Olympus LV100ND microscope. Raman spectra of AOT and LBL-transferred bilayer graphene shown in Fig. 1 were collected on a Witec alpha RAS300+ Raman system using a 488 nm laser with a laser spot size of 1 μm, and a 100× objective and 600 lines/mm grating. Other Raman spectra of transferred bilayer graphene in this work were collected on a Horiba Lab RAM HR Evolution Raman system using a 532 nm laser with a laser spot size of 1 μm, a 100× objective and a 600 line/mm grating. Thermal shock tests via flash Joule heating were conducted by using repeatable programmed electrical pulse (Zhongkejingyan, HTS5430DH). After placing the fabricated suspended graphene on the thermal shock test platform, the chamber was evacuated to a vacuum state with a pressure of ~5 Pa using a pumping system. The pulse current, pulse voltage, and heating/cooling time were carefully controlled to achieve a 10^4 Ks^{-1} heating speed and a maximum temperature as high as 1200 K. The AFM morphology images were collected on a Brucker Dimension Icon using the Scan-asyst mode. Scanning electron microscopy (SEM) images were collected using an FEI Quattro S field emission SEM at an accelerating voltage of 5 kV. TEM and SAED images were obtained on an FEI Tecnai F20 with an accelerating voltage of 200 kV. STEM images and EDS were collected on an FEI Tecnai F30 with an accelerating voltage of 300 kV. The graphene lattice temperature and radiation spectra of graphene were measured by the Renishaw inVia micro-Raman spectrometer. The voltage applied to the graphene was loaded through the DC digital source-meter 2636B (Keithley).

Data availability

All data needed to support the conclusions in the paper are presented in the manuscript and/or the Electronic Supplementary Material. Additional data related to this paper may be requested from the corresponding author upon request.

Acknowledgement

This work was supported by the National Key Research and Development Program of China (2022YFA1204900), the National Natural Science Foundation of China (22432001, 21920102004, 52021006, 52202195, 22373006, 52350209, 22502007, T2588301), Beijing National Laboratory for Molecular Sciences (BNLMS-CXTD-202001), Postdoctoral Fellowship Program of CPSF (GZB20240012), The science and technology innovation Program of Hunan Province (2025RC3120)， Innovation Research Foundation of National University of Defense Technology (23-ZZCX-JDZ-22) and New Cornerstone Science Foundation through the New Cornerstone Investigator Program and the XPLORER PRIZE.

Declaration of competing interest

All the contributing authors report no conflict of interests in this work.

Author contribution statement

H.P., S.Y.J., and X.G. conceived the project. K.C.J. carried out the synthesis of graphene. S.Y.J. and X.G. carried out the transfer and characterization of graphene. W.Y.S. and X.Y.G. collected TEM images and EDS data. S.Y.J. carried out Raman characterization. F.L and Z.L.S fabricated and measured the devices of graphene thermal light emitters. The manuscript was written by S.Y.J., X.G., H.T.L., and F. L. with the inputs from other authors. The entire work was supervised by H.P. All authors discussed the results and commented on the manuscript. All the authors have approved the final manuscript.

Informed consent

Not applicable.

Ethics statement

Not applicable.

Use of AI statement

None.

References

(1) Novoselov, K. S.; Geim, A. K.; Morozov, S. V.; Jiang, D.; Zhang, Y.; Dubonos, S. V.; Grigorieva, I. V.; Firsov, A. A. Electric Field Effect in Atomically Thin Carbon Films. *Science* **2004**, 306 (5696), 666–669.

(2) Cao, Y.; Fatemi, V.; Demir, A.; Fang, S.; Tomarken, S. L.; Luo, J. Y.; Sanchez-Yamagishi, J. D.; Watanabe, K.; Taniguchi, T.; Kaxiras, E.; Ashoori, R. C.; Jarillo-Herrero, P. Correlated Insulator Behaviour at Half-Filling in Magic-Angle Graphene Superlattices. *Nature* **2018**, 556 (7699), 80–84.

(3) Cao, Y.; Fatemi, V.; Fang, S.; Watanabe, K.; Taniguchi, T.; Kaxiras, E.; Jarillo-Herrero, P. Unconventional Superconductivity in Magic-Angle Graphene Superlattices. *Nature* **2018**, 556 (7699), 43–50.

(4) Bistritzer, R.; MacDonald, A. H. Moiré Bands in Twisted Double-Layer Graphene. *Proc. Natl. Acad. Sci.* **2011**, 108 (30), 12233–12237.

(5) Latil, S.; Henrard, L. Charge Carriers in Few-Layer Graphene Films. *Phys. Rev. Lett.* **2006**, 97 (3), 36803.

(6) Cui, T.; Mukherjee, S.; Sudeep, P. M.; Colas, G.; Najafi, F.; Tam, J.; Ajayan, P. M.; Singh, C. V.; Sun, Y.; Filleter, T. Fatigue of Graphene. *Nat. Mater.* **2020**, 19 (4), 405–411.

(7) Solís-Fernández, P.; Bissett, M.; Ago, H. Synthesis, Structure and Applications of Graphene-Based 2D Heterostructures. *Chem. Soc. Rev.* **2017**, 46 (15), 4572–4613.

(8) Lee, Y.-C.; Lin, K.-T.; Chen, H.-L. Ultra-Broadband and Omnidirectional Enhanced Absorption of Graphene in a Simple Nanocavity Structure. *Carbon* **2016**, 108, 253–261.

(9) Shen, X.; Wang, Z.; Wu, Y.; Liu, X.; He, Y.-B.; Kim, J.-K. Multilayer Graphene Enables Higher Efficiency in Improving Thermal Conductivities of Graphene/Epoxy Composites. *Nano Lett.* **2016**, 16 (6), 3585–3593.

(10) Ghosh, S.; Bao, W.; Nika, D. L.; Subrina, S.; Pokatilov, E. P.; Lau, C. N.; Balandin, A. A. Dimensional Crossover of Thermal Transport in Few-Layer Graphene. *Nat. Mater.* **2010**, 9 (7), 555–558.

(11) Kim, J.; Kim, G. G.; Kim, S.; Jung, W. Highly Enhanced Electromechanical Stability of Large-Area Graphene with Increased Interfacial Adhesion Energy by Electrothermal-Direct Transfer for Transparent Electrodes. *ACS Appl. Mater. Interfaces* **2016**, 8 (35), 23396–23403.

(12) Li, Z.; Chao, X.; Balilonda, A.; Chen, W. Scalable van Der Waals Graphene Films for Electro-Optical Regulation and Thermal Camouflage. *InfoMat* **2023**, 5 (6), e12418.

(13) Zhou, H.; Xie, T.; Taniguchi, T.; Watanabe, K.; Young, A. F. Superconductivity in Rhombohedral Trilayer Graphene. *Nature* **2021**, 598 (7881), 434–438.

(14) Liu, X.; Hao, Z.; Khalaf, E.; Lee, J. Y.; Ronen, Y.; Yoo, H.; Haei Najafabadi, D.; Watanabe, K.; Taniguchi, T.; Vishwanath, A.; Kim, P. Tunable Spin-Polarized Correlated States in Twisted Double Bilayer Graphene. *Nature* **2020**, 583 (7815), 221–225.

(15) Chen, G.; Sharpe, A. L.; Gallagher, P.; Rosen, I. T.; Fox, E. J.; Jiang, L.; Lyu, B.; Li, H.; Watanabe, K.; Taniguchi, T.; Jung, J.; Shi, Z.; Goldhaber-Gordon, D.; Zhang, Y.; Wang, F. Signatures of Tunable Superconductivity in a Trilayer Graphene Moiré Superlattice. *Nature* **2019**, 572 (7768), 215–219.

(16) Chen, G.; Jiang, L.; Wu, S.; Lyu, B.; Li, H.; Chittari, B. L.; Watanabe, K.; Taniguchi, T.; Shi, Z.; Jung, J.; Zhang, Y.; Wang, F. Evidence of a Gate-Tunable Mott Insulator in a Trilayer Graphene Moiré Superlattice. *Nat. Phys.* **2019**, 15 (3), 237–241.

(17) Huang, Y.; Sutter, E.; Shi, N. N.; Zheng, J.; Yang, T.; Englund, D.; Gao, H.-J.; Sutter, P. Reliable Exfoliation of Large-Area High-Quality Flakes of Graphene and Other Two-Dimensional Materials. *ACS Nano* **2015**, 9 (11), 10612–10620.

(18) Novoselov, K. S.; Jiang, D.; Schedin, F.; Booth, T. J.; Khotkevich, V. V.; Morozov, S. V.; Geim, A. K. Two-Dimensional Atomic Crystals. *Proc. Natl. Acad. Sci.* **2005**, 102 (30), 10451–10453.

(19) Yao, W.; Liu, H.; Sun, J.; Wu, B.; Liu, Y. Engineering of Chemical Vapor Deposition Graphene Layers: Growth, Characterization, and Properties. *Adv. Funct. Mater.* **2022**, 32 (42), 2202584.

(20) Liu, F.; Li, P.; An, H.; Peng, P.; McLean, B.; Ding, F. Achievements and Challenges of Graphene Chemical Vapor Deposition Growth. *Adv. Funct. Mater.* **2022**, 32 (42), 2203191.

(21) Zhao, J.; Ji, P.; Li, Y.; Li, R.; Zhang, K.; Tian, H.; Yu, K.; Bian, B.; Hao, L.; Xiao, X.; Griffin, W.; Dudeck, N.; Moro, R.; Ma, L.; de Heer, W. A. Ultrahigh-Mobility Semiconducting Epitaxial Graphene on Silicon Carbide. *Nature* **2024**, 625 (7993), 60–65.

(22) Berger, C.; Song, Z.; Li, T.; Li, X.; Ogbazghi, A. Y.; Feng, R.; Dai, Z.; Marchenkov, A. N.; Conrad, E. H.; First, P. N.; De Heer, W. A. Ultrathin Epitaxial Graphite: 2D Electron Gas Properties and a Route toward Graphene-Based Nanoelectronics. *J. Phys. Chem. B* **2004**, 108 (52), 19912–19916.

(23) Haigh, S. J.; Gholinia, A.; Jalil, R.; Romani, S.; Britnell, L.; Elias, D. C.; Novoselov, K. S.; Ponomarenko, L. A.; Geim, A. K.; Gorbachev, R. Cross-Sectional Imaging of Individual Layers and Buried Interfaces of Graphene-Based Heterostructures and Superlattices. *Nat. Mater.* **2012**, 11 (9), 764–767.

(24) Castellanos-Gomez, A.; Duan, X.; Fei, Z.; Gutierrez, H. R.; Huang, Y.; Huang, X.; Quereda, J.; Qian, Q.; Sutter, E.; Sutter, P. Van Der Waals Heterostructures. *Nat. Rev. Methods Primers* **2022**, 2 (1), 58.

(25) Leconte, N.; Kim, H.; Kim, H.-J.; Ha, D. H.; Watanabe, K.; Taniguchi, T.; Jung, J.; Jung, S. Graphene Bubbles and Their Role in

Graphene Quantum Transport. *Nanoscale* **2017**, 9 (18), 6041–6047.

(26) Kretinin, A. V.; Cao, Y.; Tu, J. S.; Yu, G. L.; Jalil, R.; Novoselov, K. S.; Haigh, S. J.; Gholinia, A.; Mishchenko, A.; Lozada, M.; Georgiou, T.; Woods, C. R.; Withers, F.; Blake, P.; Eda, G.; Wirsig, A.; Hucho, C.; Watanabe, K.; Taniguchi, T.; Geim, A. K.; Gorbachev, R. V. Electronic Properties of Graphene Encapsulated with Different Two-Dimensional Atomic Crystals. *Nano Lett.* **2014**, 14 (6), 3270–3276.

(27) Purdie, D. G.; Pugno, N. M.; Taniguchi, T.; Watanabe, K.; Ferrari, A. C.; Lombardo, A. Cleaning Interfaces in Layered Materials Heterostructures. *Nat Commun.* **2018**, 9 (1), 5387.

(28) Hou, Y.; Dai, Z.; Zhang, S.; Feng, S.; Wang, G.; Liu, L.; Xu, Z.; Li, Q.; Zhang, Z. Elastocapillary Cleaning of Twisted Bilayer Graphene Interfaces. *Nat. Commun.* **2021**, 12 (1), 5069.

(29) Yang, X.; Yan, M. Removing Contaminants from Transferred CVD Graphene. *Nano Res*. **2020**, 13 (3), 599–610.

(30) Pizzocchero, F.; Gammelgaard, L.; Jessen, B. S.; Caridad, J. M.; Wang, L.; Hone, J.; Bøggild, P.; Booth, T. J. The Hot Pick-up Technique for Batch Assembly of van Der Waals Heterostructures. *Nat. Commun.* **2016**, 7 (1), 11894.

(31) Dong, W.; Dai, Z.; Liu, L.; Zhang, Z. Toward Clean 2D Materials and Devices: Recent Progress in Transfer and Cleaning Methods. *Adv. Mater*. **2024**, 36 (22), 2303014.

(32) Yan, M.; Gao, X.; Qian, J.; Gao, X.; Tang, J.; Wang, Y.; Wang, Y.; Tang, J.; Zheng, L.; Jia, K.; Jia, F.; Liu, H.; Gao, G.; Peng, H. Towards Bubble-Free, Centimeter-Sized Bilayer Graphene Enabled by Backside Lamination. *J. Mater. Chem. C* **2023**, 11 (35), 11814–11821.

(33) Gao, X.; Zheng, L.; Luo, F.; Qian, J.; Wang, J.; Yan, M.; Wang, W.; Wu, Q.; Tang, J.; Cao, Y.; Tan, C.; Tang, J.; Zhu, M.; Wang, Y.; Li, Y.; Sun, L.; Gao, G.; Yin, J.; Lin, L.; Liu, Z.; Qin, S.; Peng, H. Integrated Wafer-Scale Ultra-Flat Graphene by Gradient Surface Energy Modulation. *Nat. Commun.* **2022**, 13 (1), 5410.

(34) Deng, B.; Pang, Z.; Chen, S.; Li, X.; Meng, C.; Li, J.; Liu, M.; Wu, J.; Qi, Y.; Dang, W.; Yang, H.; Zhang, Y.; Zhang, J.; Kang, N.; Xu, H.; Fu, Q.; Qiu, X.; Gao, P.; Wei, Y.; Liu, Z.; Peng, H. Wrinkle-Free Single-Crystal Graphene Wafer Grown on Strain-Engineered Substrates. *ACS Nano* **2017**, 11 (12), 12337–12345.

(35) Wu, C.; Chen, B.; Liu, H.; Song, X.; Zheng, S.; Li, Q.; Dong, Y.; Li, S.; Shao, J.; Bian, P.; Xue, J.; Huang, X.; Sun, X.; Jia, K.; Wei, W.; Gao, Z.; Sun, L.; Liu, Z. Restoring Ultra‐flat Bridgman‐fabricated Single‐crystal Cu(111) Wafers via Recrystallization Arrest Strategy for High‐quality Graphene Epitaxy. *Adv. Mater.* **2025**, 2501582.

(36) Zhao, Y.; Song, Y.; Hu, Z.; Wang, W.; Chang, Z.; Zhang, Y.; Lu, Q.; Wu, H.; Liao, J.; Zou, W.; Gao, X.; Jia, K.; Zhuo, L.; Hu, J.; Xie, Q.; Zhang, R.; Wang, X.; Sun, L.; Li, F.; Zheng, L.; Wang, M.; Yang, J.; Mao, B.; Fang, T.; Wang, F.; Zhong, H.; Liu, W.; Yan, R.; Yin, J.; Zhang, Y.; Wei, Y.; Peng, H.; Lin, L.; Liu, Z. Large-Area Transfer of Two-Dimensional Materials Free of Cracks, Contamination and Wrinkles via Controllable Conformal Contact. *Nat. Commun.* **2022**, 13 (1), 4409.

(37) Castro Neto, A. H. The Electronic Properties of Graphene. *Rev. Mod. Phys.* **2009**, 81 (1), 109–162.

(38) Hwang, E. H. Carrier Transport in Two-Dimensional Graphene Layers. *Phys. Rev. Lett.* **2007**, 98 (18).

(39) Yoon, D.; Son, Y.-W.; Cheong, H. Strain-Dependent Splitting of the Double-Resonance Raman Scattering Band in Graphene. *Phys. Rev. Lett.* **2011**, 106 (15), 155502.

(40) Huang, M.; Yan, H.; Heinz, T. F.; Hone, J. Probing Strain-Induced Electronic Structure Change in Graphene by Raman Spectroscopy. *Nano Lett.* **2010**, 10 (10), 4074–4079.

(41) Lui, C. H.; Malard, L. M.; Kim, S.; Lantz, G.; Laverge, F. E.; Saito, R.; Heinz, T. F. Observation of Layer-Breathing Mode Vibrations in Few-Layer Graphene through Combination Raman Scattering. *Nano Lett.* **2012**, 12 (11), 5539–5544.

(42) Tan, P. H.; Han, W. P.; Zhao, W. J.; Wu, Z. H.; Chang, K.; Wang, H.; Wang, Y. F.; Bonini, N.; Marzari, N.; Pugno, N.; Savini, G.; Lombardo, A.; Ferrari, A. C. The Shear Mode of Multilayer Graphene. *Nat. Mater.* **2012**, 11 (4), 294–300.

(43) Neumann, C.; Reichardt, S.; Venezuela, P.; Drögeler, M.; Banszerus, L.; Schmitz, M.; Watanabe, K.; Taniguchi, T.; Mauri, F.; Beschoten, B.; Rotkin, S. V.; Stampfer, C. Raman Spectroscopy as Probe of Nanometre-Scale Strain Variations in Graphene. *Nat. Commun.* **2015**, 6 (1), 8429.

(44) Yao, Y.; Huang, Z.; Xie, P.; Lacey, S. D.; Jacob, R. J.; Xie, H.; Chen, F.; Nie, A.; Pu, T.; Rehwoldt, M.; Yu, D.; Zachariah, M. R.; Wang, C.; Shahbazian-Yassar, R.; Li, J.; Hu, L. Carbothermal Shock Synthesis of High-Entropy-Alloy Nanoparticles. *Science* **2018**, 359 (6383), 1489–1494.

(45) Yao, Y.; Huang, Z.; Xie, P.; Wu, L.; Ma, L.; Li, T.; Pang, Z.; Jiao, M.; Liang, Z.; Gao, J.; He, Y.; Kline, D. J.; Zachariah, M. R.; Wang, C.; Lu, J.; Wu, T.; Li, T.; Wang, C.; Shahbazian-Yassar, R.; Hu, L. High Temperature Shockwave Stabilized Single Atoms. *Nat. Nanotechnol.* **2019**, 14 (9), 851–857.

(46) Liu, Q.; Xu, W.; Li, X.; Zhang, T.; Qin, C.; Luo, F.; Zhu, Z.; Qin, S.; Zhu, M.; Novoselov, K. S. Electrically-Driven Ultrafast out-of-Equilibrium Light Emission from Hot Electrons in Suspended Graphene/hBN Heterostructures. *Int. J. Extrem. Manuf.* **2024**, 6 (1), 015501.

(47) Kim, Y. D.; Kim, H.; Cho, Y.; Ryoo, J. H.; Park, C.-H.; Kim, P.; Kim, Y. S.; Lee, S.; Li, Y.; Park, S.-N.; Shim Yoo, Y.; Yoon, D.; Dorgan, V. E.; Pop, E.; Heinz, T. F.; Hone, J.; Chun, S.-H.; Cheong, H.; Lee, S. W.; Bae, M.-H.; Park, Y. D. Bright Visible Light Emission from Graphene. *Nat. Nanotechnol.* **2015**, 10 (8), 676–681.

(48) Luo, F.; Fan, Y.; Peng, G.; Xu, S.; Yang, Y.; Yuan, K.; Liu, J.; Ma, W.; Xu, W.; Zhu, Z. H.; Zhang, X.-A.; Mishchenko, A.; Ye, Y.; Huang, H.; Han, Z.; Ren, W.; Novoselov, K. S.; Zhu, M.; Qin, S. Graphene Thermal Emitter with Enhanced Joule Heating and Localized Light Emission in Air. *ACS Photonics* **2019**, 6 (8), 2117–2125.

(49) Miyoshi, Y.; Fukazawa, Y.; Amasaka, Y.; Reckmann, R.; Yokoi, T.; Ishida, K.; Kawahara, K.; Ago, H.; Maki, H. High-Speed and on-Chip Graphene Blackbody Emitters for Optical Communications by Remote Heat Transfer. *Nat Commun.* **2018**, 9 (1), 1279.

(50) Freitag, M.; Chiu, H.-Y.; Steiner, M.; Perebeinos, V.; Avouris, P. Thermal Infrared Emission from Biased Graphene. *Nat. Nanotechnol.* **2010**, 5 (7), 497–501.

(51) Gao, L.; Ren, W.; Xu, H.; Jin, L.; Wang, Z.; Ma, T.; Ma, L.-P.; Zhang, Z.; Fu, Q.; Peng, L.-M.; Bao, X.; Cheng, H.-M. Repeated Growth and Bubbling Transfer of Graphene with Millimetre-Size Single-Crystal Grains Using Platinum. *Nat. Commun.* **2012,** 3 (1), 699.

Electronic Supplementary Material

Wafer-scale interface-clean few-layer graphene stacks enabled by active oxygen treatment

Siyi Ji[1,2,§], Xin Gao[3,§], Zhilong Shang[4,5,§], Weiyu Sun[3,6], Xiaoyin Gao[3], Kaicheng Jia[2], Mengwei Li[1], Junqiang Wang[1], Hongtao Liu[3*], Fang Luo[4,5*], and Hailin Peng[2,3*]

[1] *Academy for Advanced Interdisciplinary Research, North University of China, Taiyuan 030051, China*
[2] *Beijing Graphene Institute, Beijing 100095, China*
[3] *Center for Nano chemistry, Beijing Science and Engineering Center for Nanocarbons, Beijing National Laboratory for Molecular Sciences, College of Chemistry and Molecular Engineering, Peking University, Beijing 100871, China*
[4] *College of Advanced Interdisciplinary Studies& Hunan Provincial Key Laboratory of Novel Nano-optoelectronic Information Materials and Devices, National University of Defense Technology, Changsha 410073, China*
[5] *Nanhu Laser Laboratory, National University of Defense Technology, Changsha 410073, China*
[6] *Academy for Advanced Interdisciplinary Studies, Peking University, Beijing 100871, China*
[§] *Siyi Ji, Xin Gao, and Zhilong Shang contributed equally to this work.*

Address correspondence to Hongtao Liu, htliu-cnc@pku.edu.cn; Fang Luo, luofang@nudt.edu.cn; Hailin Peng, hlpeng@pku.edu.cn

Supporting information to https://doi.org/10.26599/NR.2026.94908543

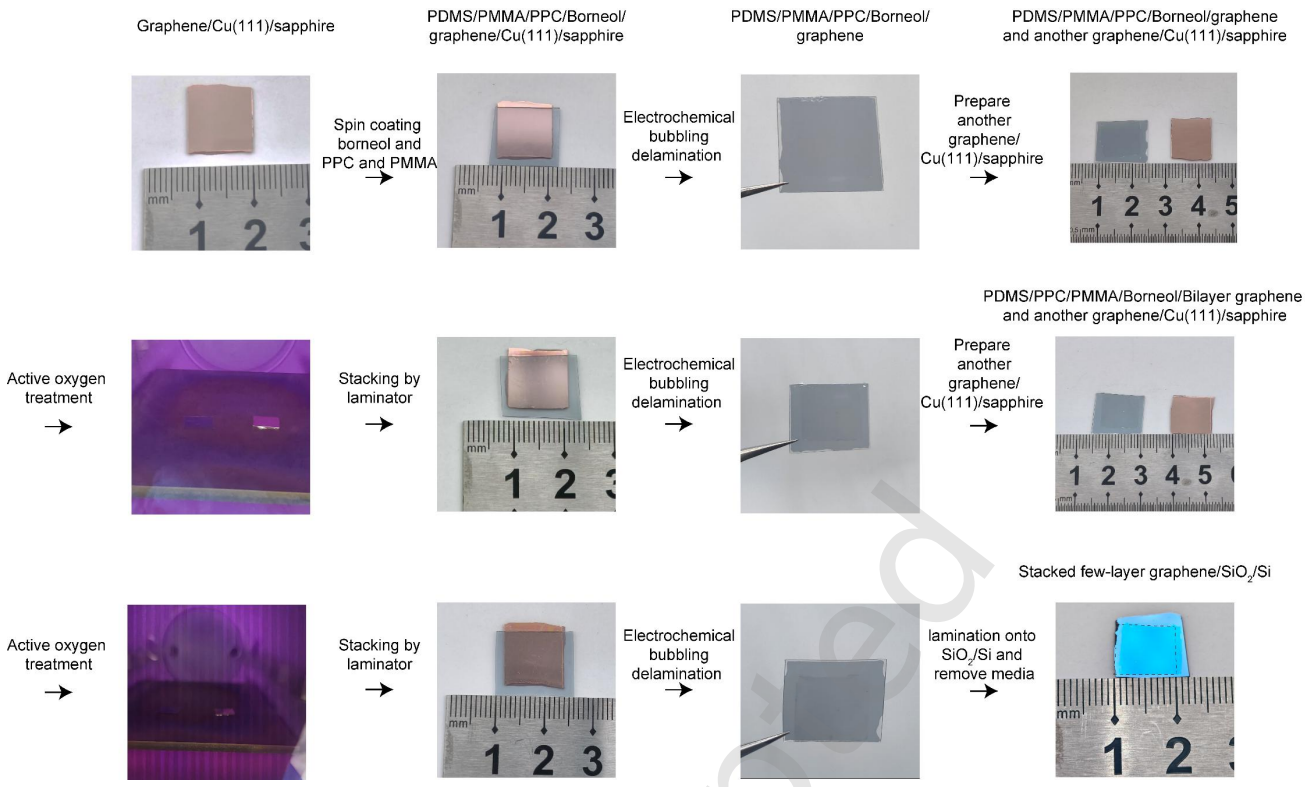

Fig. S1 Step-by-step fabrication of few-layer graphene by AOT method.

1. A graphene wafer was cut into several pieces. One piece was sequentially spin-coated with borneol, PPC, and PMMA, then laminated with PDMS obtaining a PDMS/PMMA/PPC/Borneol/ graphene/Cu (111)/sapphire composite structure.
2. The PDMS/PMMA/PPC/Borneol/graphene film was delaminated from the growth substrate by electrochemical bubbling method. After rinsing with deionized water, the composite films were fully dried in air at room temperature.
3. The delaminated graphene film and another piece of graphene/growth substrate were cleaned with active oxygen before stacking.
4. These two pieces of graphene were laminated together to obtain PDMS/PMMA/PPC/Borneol/bilayer graphene/Cu (111)/sapphire.
5. The PDMS/PMMA/PPC/Borneol/bilayer graphene film was delaminated from the growth substrate by electrochemical bubbling method.
6. Repeat step 3–5 to obtain PDMS/PMMA/PPC/Borneol/few-layer graphene composite structure.
7. The PDMS/PMMA/PPC/Borneol/few-layer graphene was laminated onto the target substrate, such as SiO_2/Si substrate.
8. The PDMS was released at 180 °C, and the PMMA/PPC/Borneol/few-layer graphene/SiO_2/Si was baked at 180 °C for 2 h. Finally, the PMMA/PPC/Borneol was removed with the vapor of hot acetone, leaving the few-layer graphene on the target substrate.

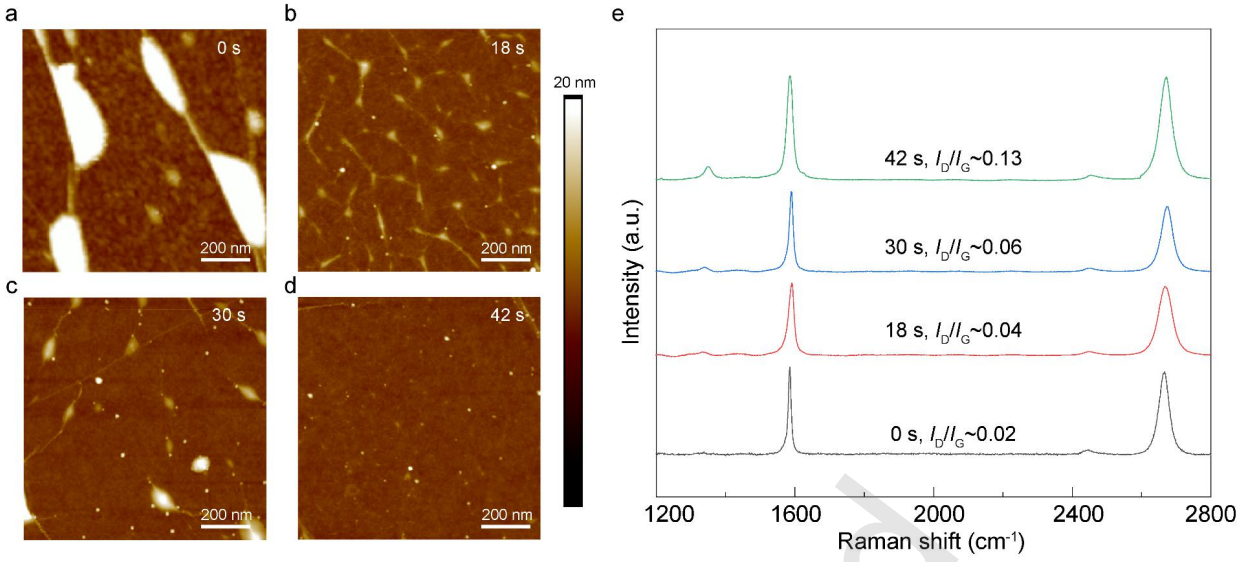

Fig. S2 The relationship of interface bubble and D/G ratio with exposure time of AOT. (a-d) AFM characterization of the morphology of interfacial bubbles in stacked bilayer graphene with different exposure time. (e) The Raman spectra and D/G ratio of stacked bilayer graphene with different exposure time. To achieve the balance between graphene defects and interface bubble, we choose the treatment time of 42 s at 30 W and an oxygen flow of 5 sccm.

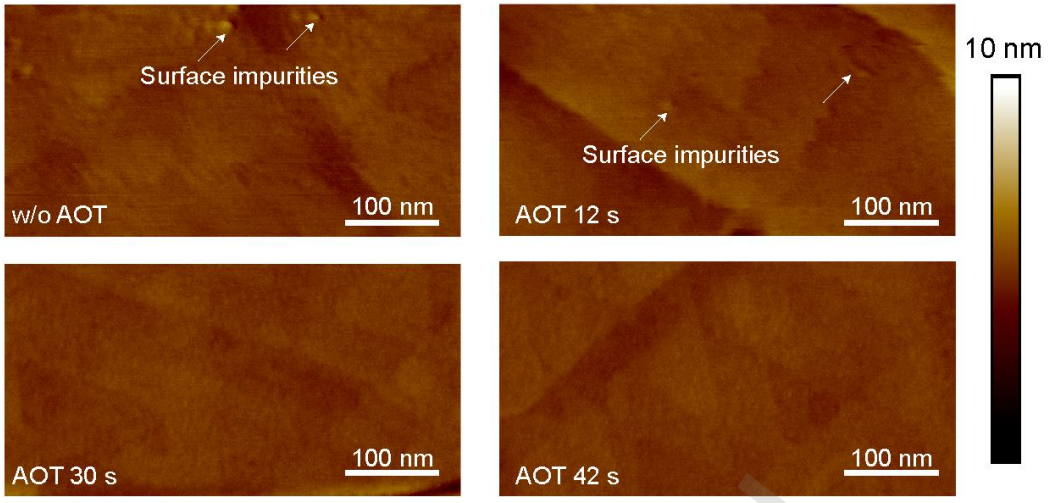

Fig. S3 The influence of using AOT cleaning on the surface morphology of as-grown graphene. The white arrows indicate surface impurities such as amorphous carbon and adsorbed contamination. After 42 s AOT, the triangularly oriented slip lines of copper substrate become clearly visible, indicating the effective removal of contaminants by AOT.

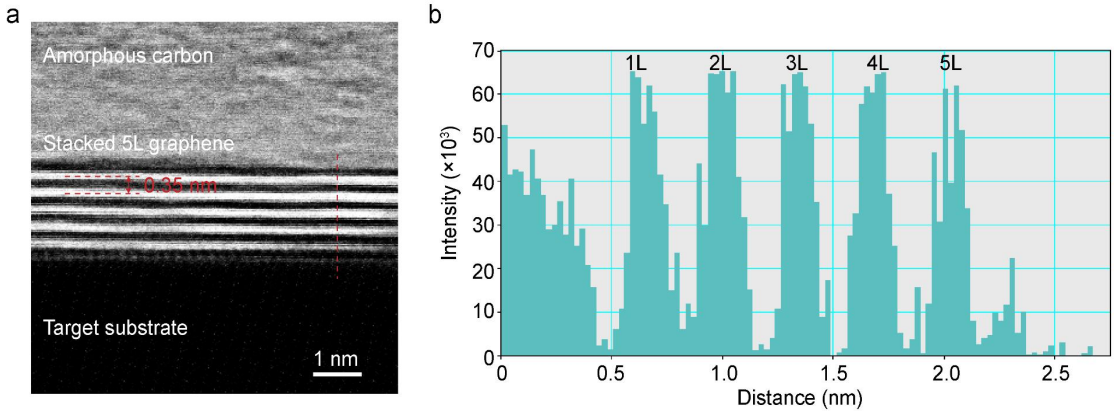

Fig. S4 The cross-sectional STEM image of AOT-stacked five-layer graphene. (a) Cross-sectional STEM image of AOT-stacked five-layer graphene. (b) Intensity line profile along the vertical dash line in (a) resolving the five graphene layers.

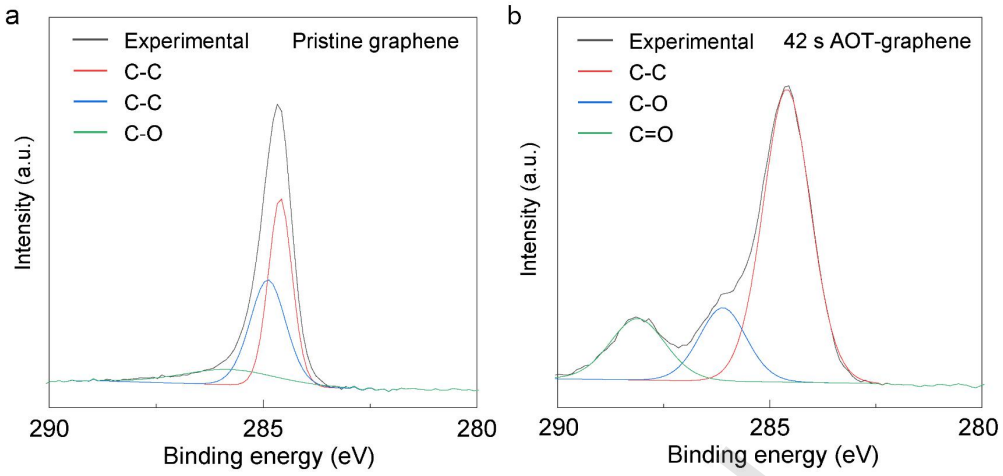

Fig. S5 X-ray photoelectron spectroscopy of pristine graphene (a) and AOT-graphene with exposure time of 42s (b). After AOT 42 s, the graphene was slightly functionalized with oxygen-containing groups.

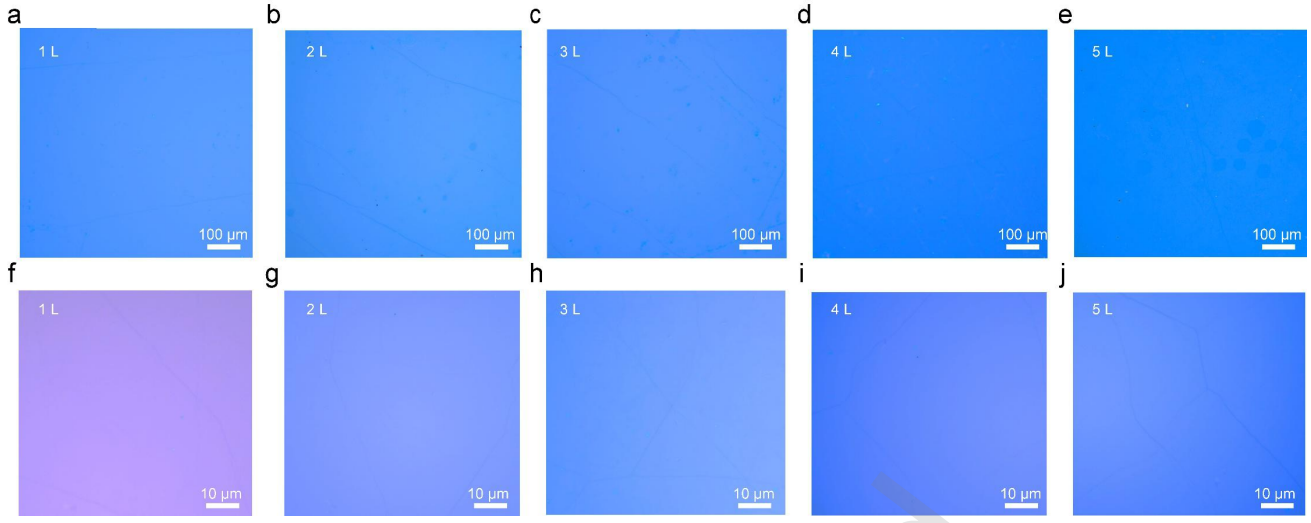

Fig. S6 Optical microscopy images of few-layer graphene stacked by AOT method. (**a–e**) Low magnification optical microscopy images of monolayer to five-layer graphene stacked by AOT method. (**f–j**) Large magnification optical microscopy images of monolayer to five-layer graphene stacked by AOT method. Whether in large or small areas, AOT graphene are uniform without bubbles, wrinkles and damages.

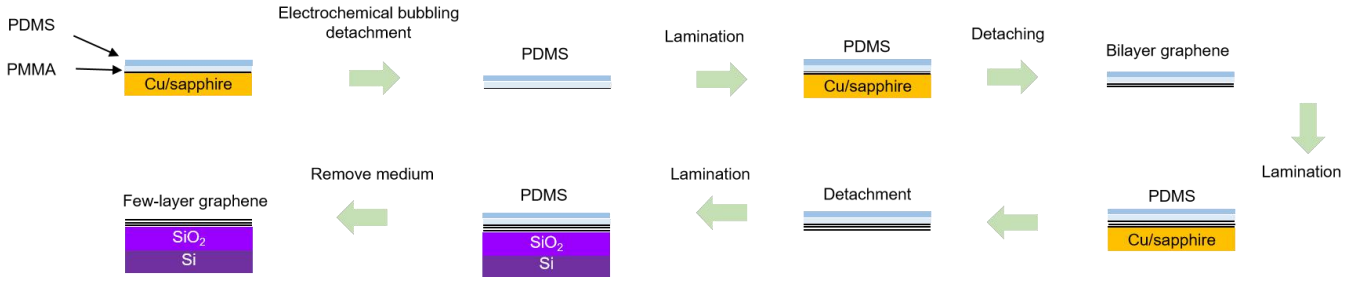

Fig. S7 Schematic illustration of fabrication of few-layer graphene by conventional LBL method. The conventional layer-by-layer transfer method can avoid interface contacting with polymer. However, amorphous carbon and adsorbed contaminant may be trapped at the interface.

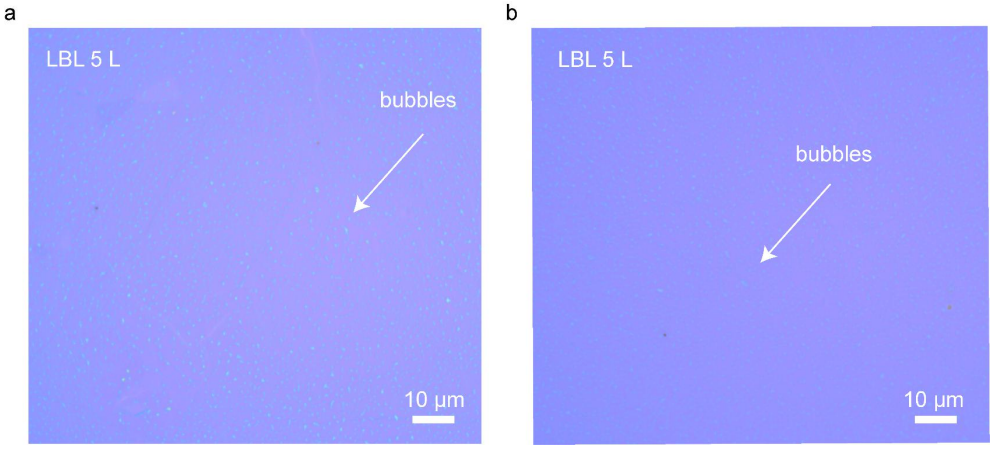

Fig. S8 Optical microscopy images of five-layer graphene transferred by conventional LBL method. (**a–b**) Optical microscopy images of five-layer graphene transferred by conventional LBL method. The white arrows represent the interfacial bubbles.

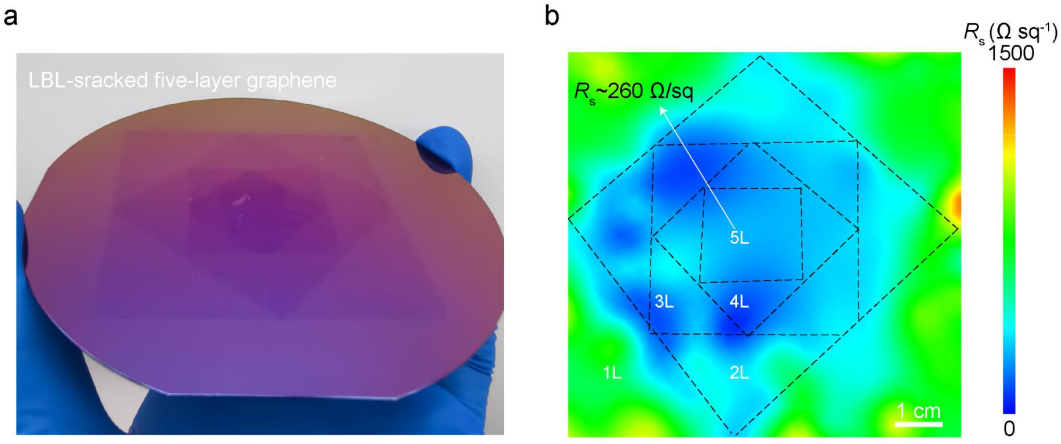

Fig. S9 Characterization of LBL-stacked five-layer graphene. (a) The optical image of LBL-stacked five-layer graphene. The damage observed in the five-layer region is presumably attributed to rupture of interfacial bubbles and/or weak interface coupling caused by repeated stacking and the less controllable removal of polymer residues. (b) The sheet resistance map of the LBL-stacked five-layer graphene.

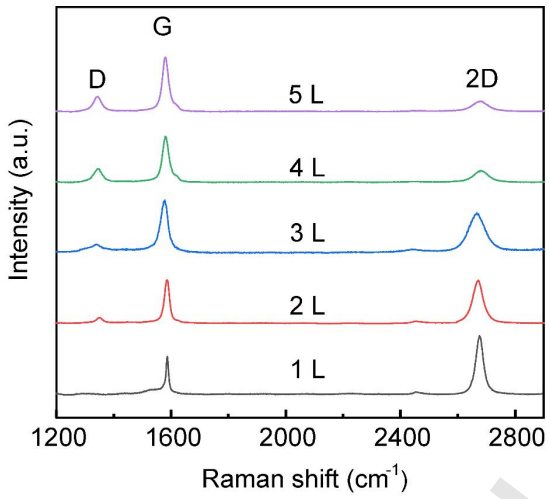

Fig. S10 Raman spectra of AOT-stacked graphene. Raman spectra of monolayer to five-layer graphene transferred by AOT method. The broadened and decreased 2D peaks of as-fabricated few-layer graphene indicates pronounced interlayer coupling and clean interface between the stacked layers.

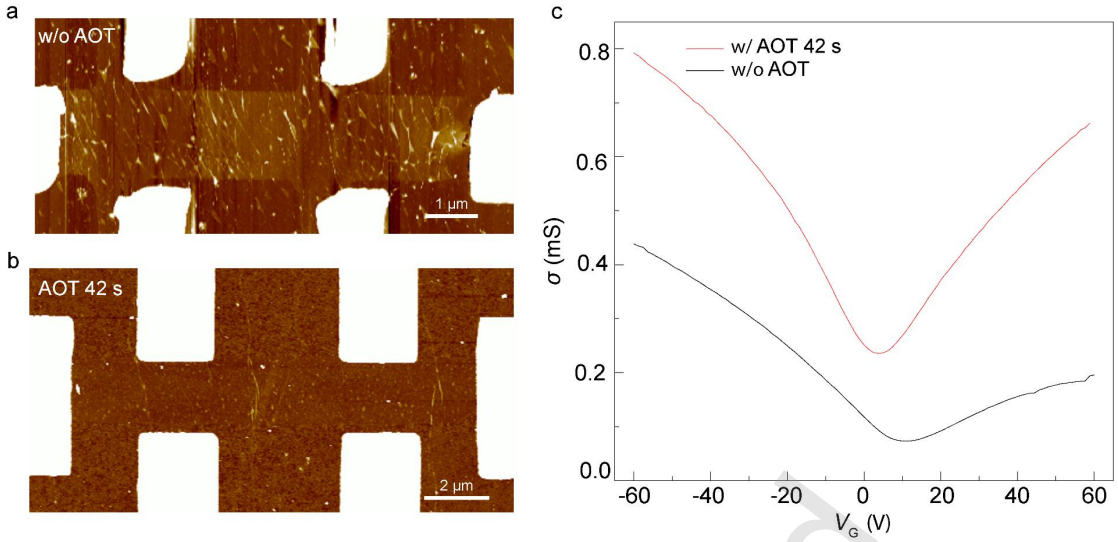

Fig. S11 The influence of interface bubbles on electrical performance of stacked bilayer graphene. (a, b) AFM images showing the morphology of the devices fabricated from LBL-stacked (a) and AOT-stacked (b) bilayer graphene, respectively. (c) Typical transfer curves of the graphene field effect transistors. The four-probe hole mobility of graphene is ~2500 cm^2 V^{-1} s^{-1} and 1200 cm^2 V^{-1} s^{-1} for the stacked bilayer graphene with and without AOT, respectively.

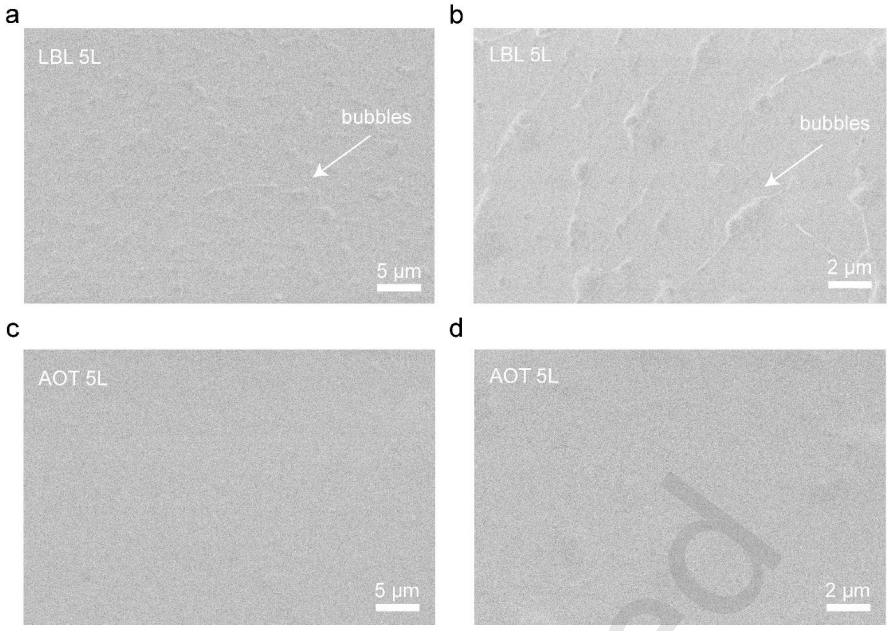

Fig. S12 SEM images of few-layer graphene fabricated with and without AOT. (**a, b**) SEM images of five-layer graphene obtained by conventional LBL transfer method. The arrows indicate the interfacial bubbles trapped between graphene layers. (**c, d**) SEM images of five-layer graphene obtained by AOT transfer method.

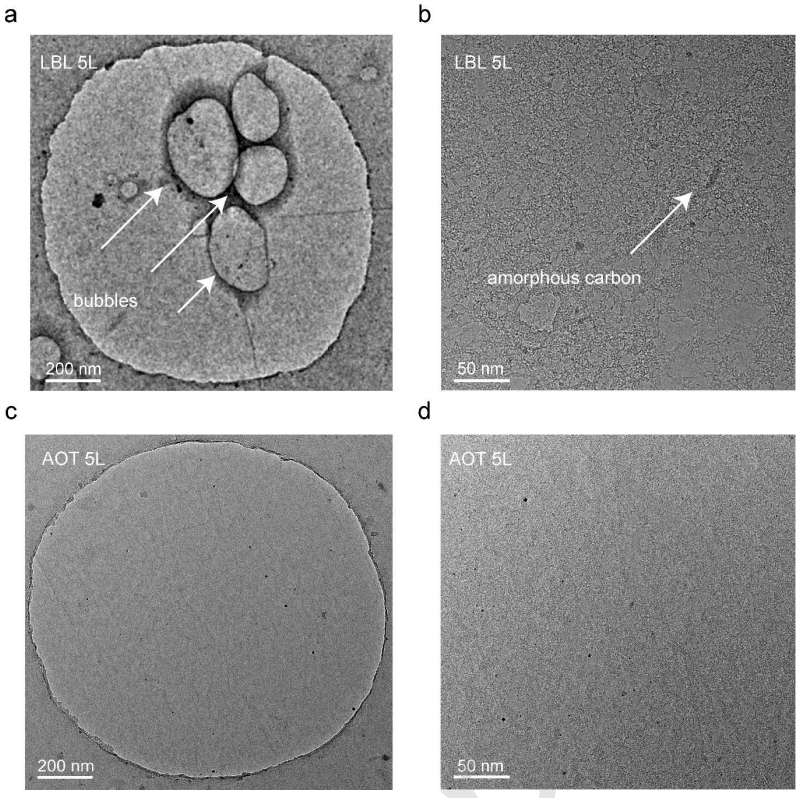

Fig. S13 TEM characterization of few-layer graphene. (**a**) Low magnification TEM image of five-layer graphene obtained by conventional LBL transfer method (in Fig. 2c). The arrows indicate the interfacial bubbles. (**b**) Large magnification TEM image of five-layer graphene obtained by conventional LBL transfer method. The arrows indicate the amorphous carbon. (**c**) Low magnification TEM images of five-layer graphene obtained by AOT method. (**d**) Large magnification TEM image of five-layer graphene obtained by AOT method.

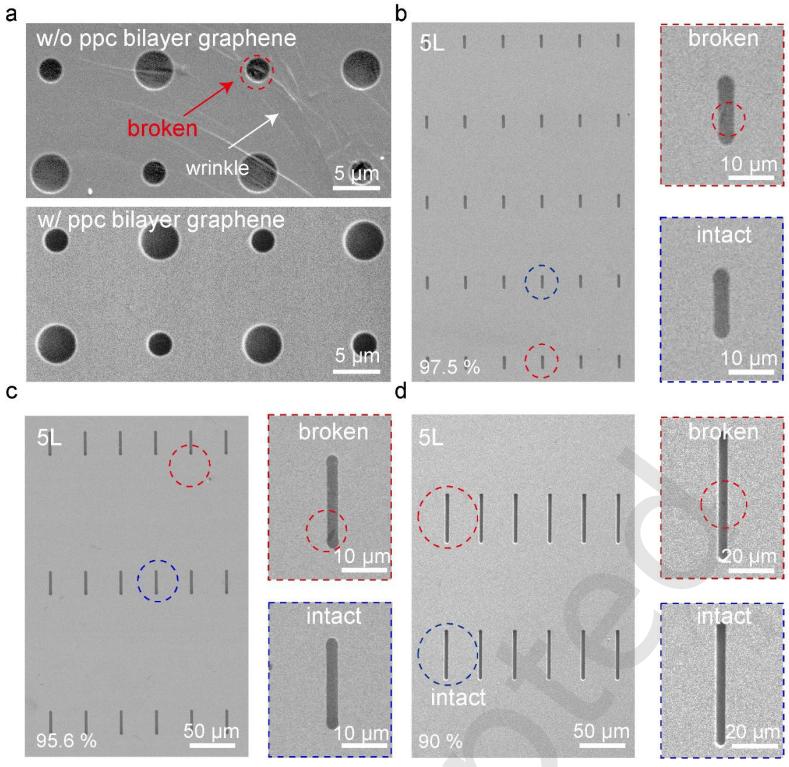

Fig. S14 SEM characterization of suspended few-layer graphene. (**a**) As-transferred bilayer graphene with and without using the transfer medium PPC on holey substrates. The conformal contact provided by PPC ensures the structural integrity of the transferred graphene and avoid the wrinkles. (**b–d**) Structural integrity of suspended graphene transferred with AOT method across various hole sizes, (**b**) 3 × 10 μm^2, (c) 3 × 20 μm^2, (d) 3 × 40 μm^2. The red dash line boxes represent magnified images of the broken holes highlighted with red circles in the low-magnification images. The blue dash line boxes represent magnified images of the intact holes marked with blue circles in the low-magnification images.

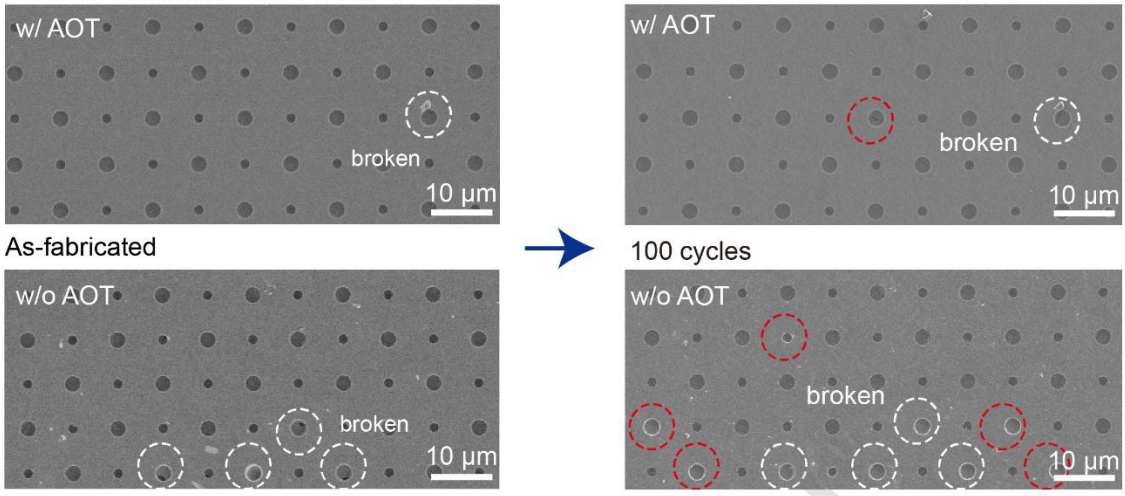

Fig. S15 SEM characterization of suspended bilayer graphene before and after thermal shock cycles. SEM images of bilayer graphene transferred onto holey substrates with and without AOT captured before and after thermal shock. The white dashed circles represent the damage before the thermal shock, while the red dashed circles highlight the additional damage after the thermal shock. Graphene transferred by AOT exhibits superior thermal shock resistance compared with that transferred by the conventional LBL.

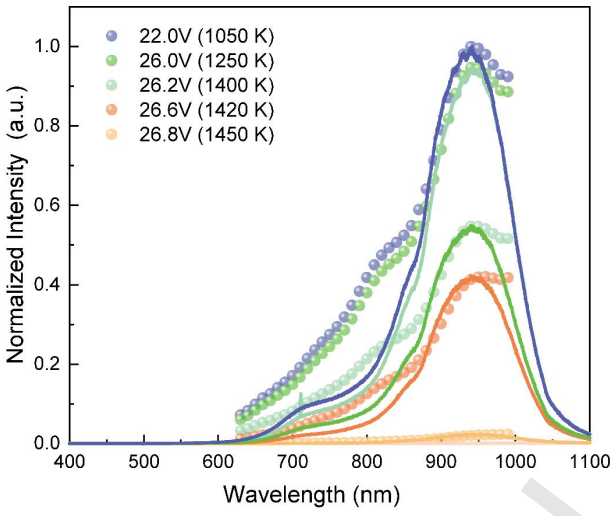

Fig. S16 Electron temperature of five-layer graphene at different bias voltages. The straight line represents the measured curve, while the dotted line corresponds to the fitted curve.

First, by fitting the experimentally measured emission spectra, we extracted the electron temperature of graphene under an applied voltage of 26.8 V, corresponding to an electrical power density of 7.49 kW/cm^2. The fitted electron temperature is T = 1450 K, as shown in the figure (Fig. S16).

Second, according to the Stefan–Boltzmann law,

$$J = \varepsilon\sigma T^4,$$

where ε is the emissivity, $\sigma = 5.67 \times 10^{-8}\ \mathrm{W\,m^{-2}\,K^{-4}}$ is the Stefan–Boltzmann constant, and T is the electron temperature derived from the emission spectra. For five-layer graphene, the emissivity is taken as $\varepsilon = 0.023 \times 5 = 0.115$. Based on this relation, the thermal radiation power density of graphene at an injected electrical power density of 7.49 kW/cm² is calculated to be $2.883 \times 10^{-3}\ \mathrm{kW/cm^2}$.

Finally, the thermal radiation efficiency of our suspended graphene device is calculated to be 3.85×10^{-4}, which is about 100 times than graphene emitters on SiO_2/Si (*Nature Nanotech* 2015, 10, 676–681).

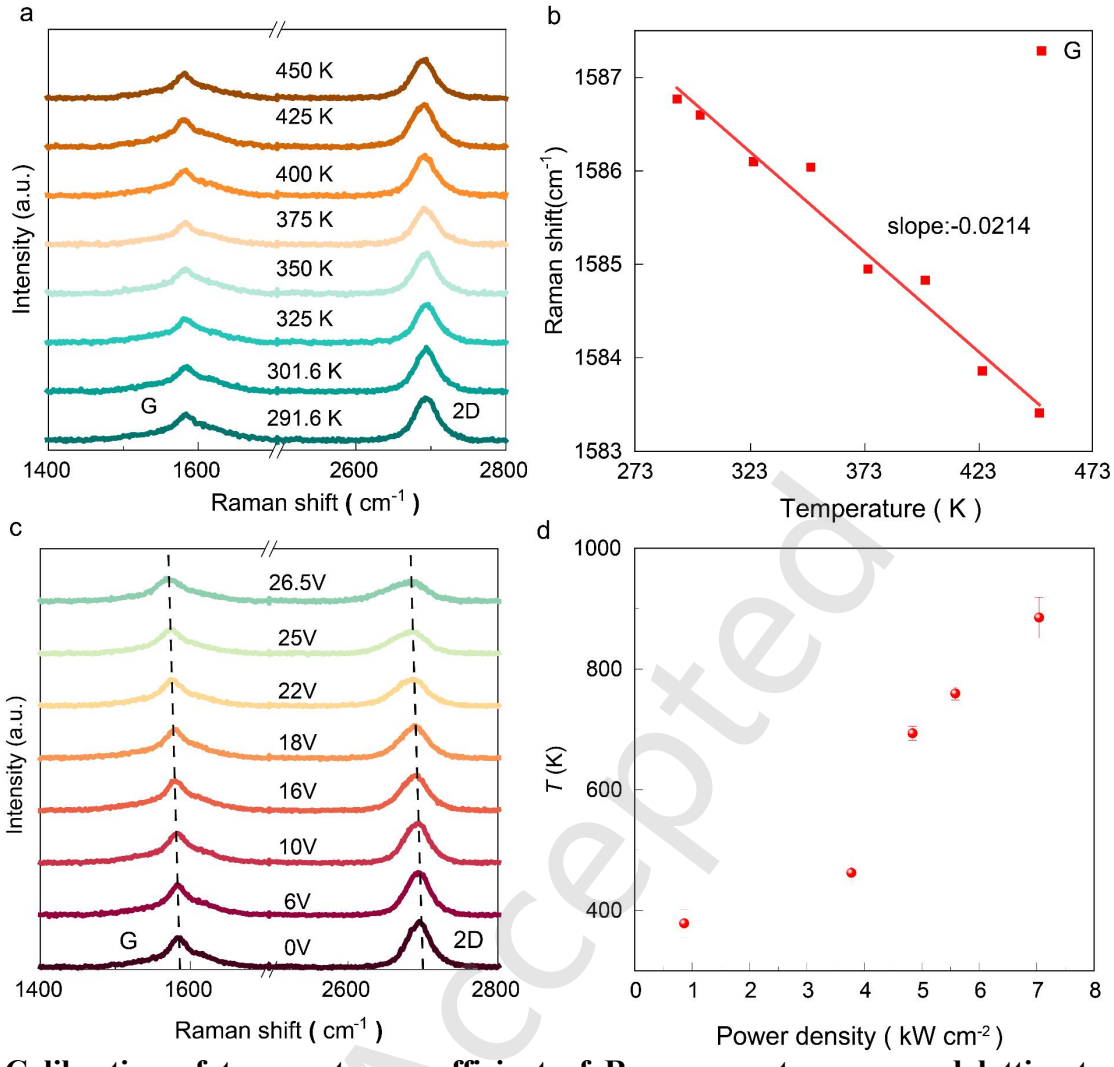

Fig. S17 Calibration of temperature coefficient of Raman spectroscopy and lattice temperature measurement of graphene under current-induced heating. (a) Raman spectra of graphene measured at different environmental temperatures, showing the monotonic redshift of G and 2D peaks with increasing temperature. (b) Extracted G-peak position ω_G as a function of environmental temperature T, together with a linear fit. The data follow the relation $\Delta\omega = \chi\Delta T$, where $\Delta\omega$ is the peak shift relative to the reference temperature and χ is the temperature coefficient ($cm^{-1}\cdot K^{-1}$). The plot shows the fitted line and its 95% confidence interval (if applicable). The fitted slope χ_G gives the temperature coefficient of the G peak. (c) Raman spectra of the graphene device under different bias voltages V, showing the redshift of G and 2D peaks with increasing voltage. (d) Graphene lattice temperature $T_{\text{lattice}}(V)$, plotted as a function of input power density, obtained by converting the voltage-induced peak shifts in (c), using the temperature coefficient extracted in (b). The conversion follows $\Delta T = \Delta\omega/\chi$, calculated from G peaks.

Table S1. The comparison of power density of graphene emitters.

No.	**Power density** (kW/cm^2)	Device structure	Radiation spectrum (nm)	Reference
1	453	hBN/Graphene/hBN	400-1100	*Nano Letters* **2018** 18, 934
2	19.75	3-layer graphene	1100-1500	*Nat Commun* **2018**, 9, 1279
3	12	graphene based field-effect LED	450-750	*Nat Commun* **2015**, 6, 7767
4	18.6	graphene	1330-2480	*Nature Nanotech* **2010**,5, 497
5	7.04	5-layer graphene	600-1100	This work

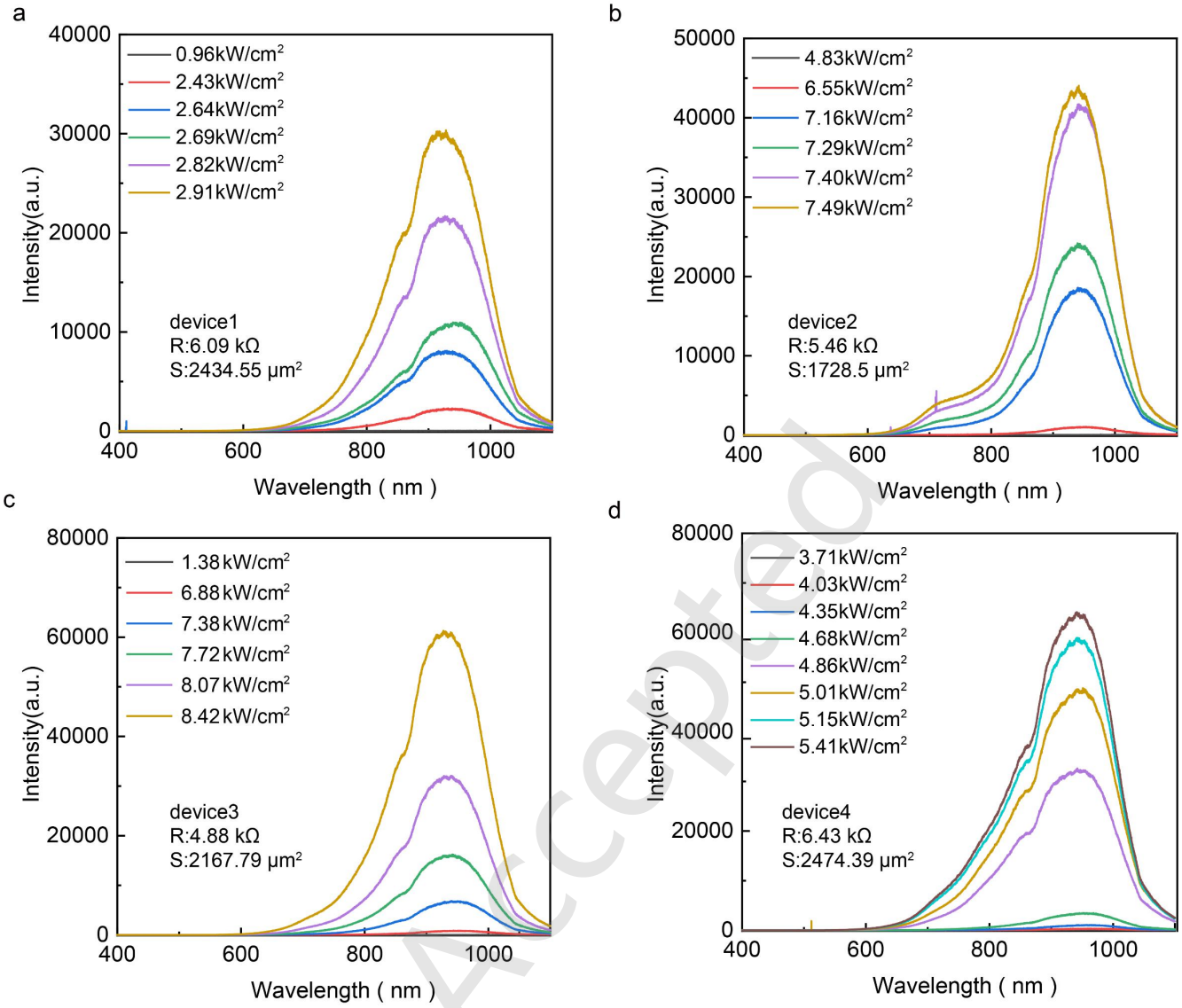

Fig. S18 Thermal emission spectra of AOT-stacked five-layer graphene with different dimensions.

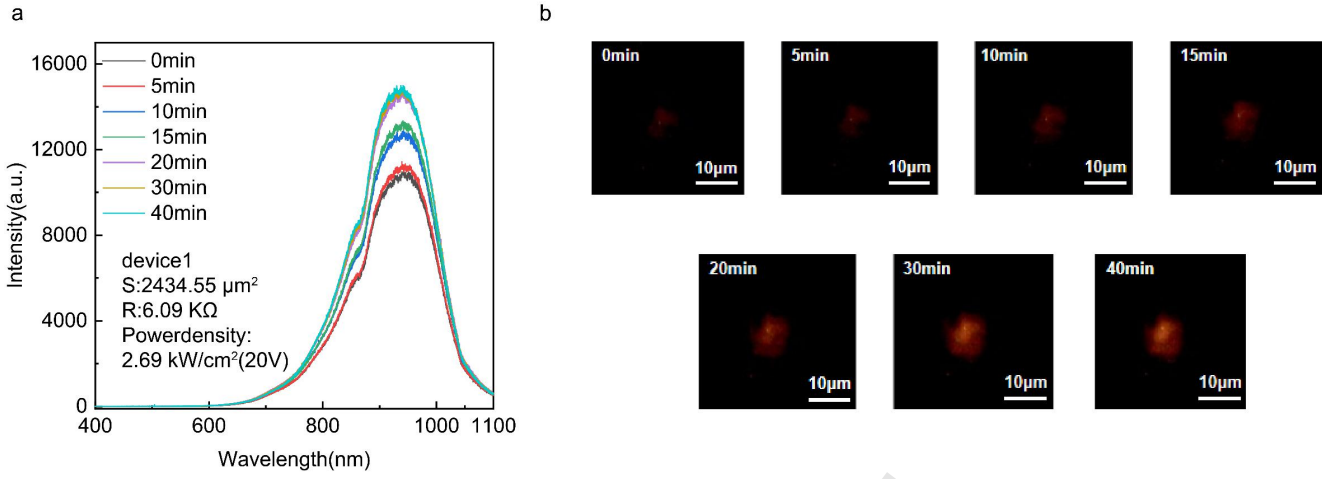

Fig. S19 Thermal emission spectra of devices 1 measured at a fixed applied voltage. (a) Emission spectrum of device 1. (b) Emission brightness as a function of measurement time.